We are IntechOpen,
the world's leading publisher of Open Access books
Built by scientists, for scientists

5,900
Open access books available

145,000
International authors and editors

180M
Downloads

154
Countries delivered to

Our authors are among the

TOP 1%
most cited scientists

12.2%
Contributors from top 500 universities

BOOK CITATION INDEX
CLARIVATE ANALYTICS
INDEXED

WEB OF SCIENCE™

Selection of our books indexed in the Book Citation Index
in Web of Science™ Core Collection (BKCI)

Interested in publishing with us?
Contact book.department@intechopen.com

Numbers displayed above are based on latest data collected.
For more information visit www.intechopen.com

Challenges and Opportunities of Optical Wireless Communication Technologies

Isiaka Alimi, Ali Shahpari, Artur Sousa,
Ricardo Ferreira, Paulo Monteiro and
António Teixeira

Additional information is available at the end of the chapter

Abstract

In this chapter, we present various opportunities of using optical wireless communication (OWC) technologies in each sector of optical communication networks. Moreover, challenges of optical wireless network implementations are investigated. We characterized the optical wireless communication channel through the channel measurements and present different models for the OWC link performance evaluations. In addition, we present some technologies for the OWC performance enhancement in order to address the last-mile transmission bottleneck of the system efficiently. The technologies can be of great help in alleviating the stringent requirement by the cloud radio access network (C-RAN) backhaul/fronthaul as well as in the evolution toward an efficient backhaul/fronthaul for the 5G network. Furthermore, we present a proof-of-concept experiment in order to demonstrate and evaluate high capacity/flexible coherent PON and OWC links for different network configurations in the terrestrial links. To achieve this, we employ advanced modulation format and digital signal processing (DSP) techniques in the offline and real-time mode of the operation. The proposed configuration has the capability to support different applications, services, and multiple operators over a shared optical fiber infrastructure.

Keywords: atmospheric turbulence, bit error rate (BER) performance, channel characterization, ergodic capacity, free-space optical (FSO) communication, relay-assisted transmission, RF/FSO technology, scintillation index

1. Introduction

The Internet is experiencing high growth with varieties of bandwidth-intensive mobile applications on an unprecedented scale. One of the potential reasons for the growth is the Internet of Things (IoT) technologies that have brought exceptional revolutions into the number of devices

in the network. Conceptually, IoT entails ubiquitous existence of a variety of *things* such as mobile phones, sensors, actuators, and radio-frequency identification (RFID) tags. These entities are capable of interacting with each other as well as cooperating with their neighbors in order to accomplish common goals via unique addressing scheme [1]. It is envisaged that by the year 2020, billions of devices with an average of six to seven devices per person will be connected to the Internet [2]. The fifth generation (5G) wireless communication systems in which millimeter-wave (mm-wave) and massive multiple-input multiple-output (M-MIMO) antenna technologies are expected to be integrated are the promising solutions for supporting the huge amount of anticipated devices. However, the radio-frequency (RF)-based wireless mobile technologies transmission speeds are limited by the available RF spectrum in the regulated RF spectrum. This is due to various innovative wireless technologies and standards like WiMAX (IEEE 802.16), UWB (IEEE 802.15), Wi-Fi (IEEE 802.11), iBurst (IEEE 802.20), the cellular-based 3G and 4G [3]. Moreover, because of various advanced technologies being employed in the optical communications, there have been considerable advancements in the optical system capacity, network reach, and number of supported users. For example, the optical-fiber-based broadband network architectures like fiber to the home (FTTH) and fiber to the building (FTTB) present commercial solutions to the communication barriers by progressively rendering services closer to the customers via the passive optical network (PON) technologies such as gigabit PON (GPON), 10Gbps PON (XG-PON), and Ethernet PON (EPON). Currently, one of the major challenges is the capability to support various service requirements so as to achieve elastic and ubiquitous connections [4]. Consequently, convergence of wireless and optical networks is highly essential for cost-effective and pervasive network penetration for the next-generation network (NGN). The convergence will help in exploiting the mobility benefit offered by the wireless connectivity and the inherent bandwidth provided by the optical systems. This will help in achieving the anticipated capacity and energy-efficiency objectives of the NGNs [3]. Furthermore, optical wireless communication (OWC) system is one of attractive broadband access technologies that offer high speed as well as improved capacity. Consequently, the OWC can attend to the bandwidth requirements of different services and applications of the NGNs at relatively low cost [3, 5].

The OWC can be an alternative and/or complementary technology for the current wireless RF solutions. For instance, OWC operating at 350–1550 nm wavelength band can offer high data rate of about 30 Gb/s data rate. This advantage makes it an attractive solution for addressing the prevailing "last mile" and "last-leg" problems in the access network. Furthermore, in mobile communication, resources re-use is an important requirement in order to enhance the network coverage and capacity. OWC technology is able to meet this requirement with the aid of spatial diversity [5, 6]. OWC link can be of different configurations such as

1. Directed line of sight (LOS)

2. Nondirected LOS

3. Diffuse

4. Quasidiffuse

5. Multispot LOS

Out of these configurations, the LOS links have the highest data rates, lowest bit error rate (BER) performance, and less complex protocol. These features make LOS link the extensively employed configuration in the outdoor applications. Nevertheless, the major deficiencies of the LOS link are lack of mobility and susceptibility to blockage. The diffuse and nondirected LOS configurations, on the other hand, give better mobility advantages and are less susceptible to shading. However, noise, path loss, and multipath-induced dispersion relatively hinder their achievable data rate for high-speed links. Intensity modulation/direct detection (IM/DD) is the most widely used scheme in OWC systems. Furthermore, coherent scheme can also be employed to enhance channel usage. Implementation of coherent scheme relatively improves system performance at the expense of increased system complexity. This can be attributed to the fact that, precise wave-front matching between the incoming signal and the local oscillator (LO) is required to guarantee efficient coherent reception. Furthermore, DD application is uncomplicated as just low-cost transceiver devices are required without the necessity for the intricate high-frequency circuit designs relative to coherent systems [5, 6].

1.1. Block diagram of OWC system

A terrestrial OWC system consists of the transmitter, channel, and receiver. **Figure 1** illustrates a schematic of a terrestrial OWC system. The source at the transmitter generates information waveforms which are modulated onto an optical carrier. The optical field produced is then radiated over the atmospheric channel to the destination. The optically collected field at the receiver is then transformed to an electrical current. The detected electrical current is processed in order to recover the original transmitted information [8]. However, the received information may not be an exact replica of the original transmitted information because of the transmission loss experienced over the channel by the signal. This factor significantly limits the performance of wireless communications systems.
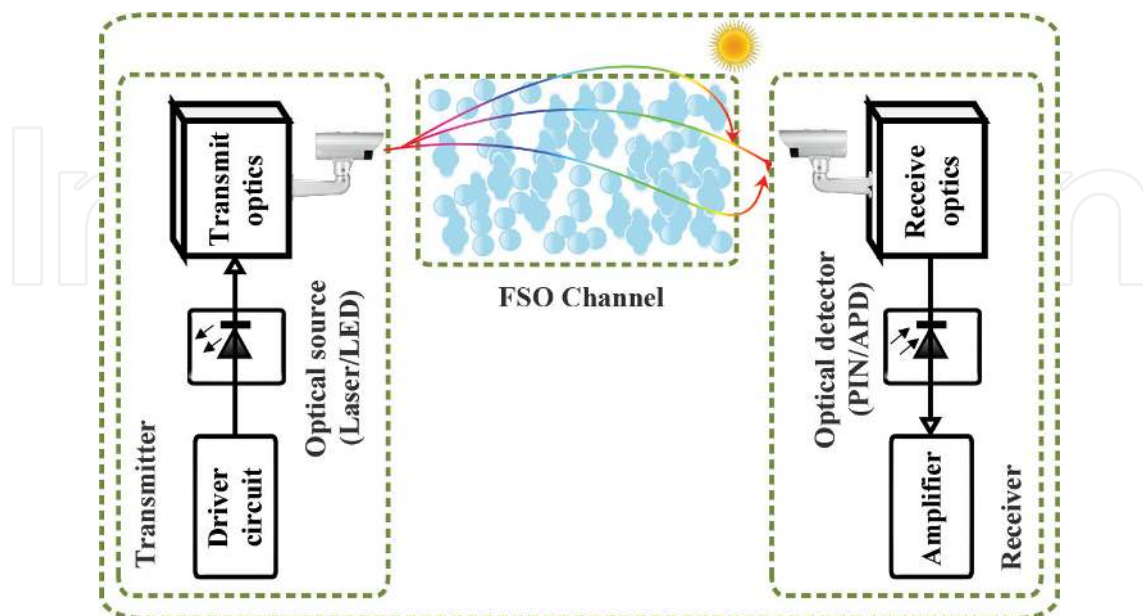

Figure 1. Block diagram of a terrestrial OWC system.

The transmission loss is mainly due to the resultant effects of scattering and absorption which are being introduced by the molecular constituents and aerosols along the transmission path. Therefore, scattering and wavelength-dependent absorption are the key components of atmospheric attenuation. Since absorption is a function of wavelength and wavelength selective, there are a range of wavelength windows that experience comparatively minimal absorptions. These transmittance windows in the absorption spectra of the atmospheric molecules are as shown in **Figure 2**.

In general, the wavelength ranges of 780–850 nm and 1520–1600 nm commonly used in the current OWC equipment are located in the atmospheric transmission windows where molecular absorption is negligible. This helps in mitigating the atmospheric absorption losses. Furthermore, certain wavelength windows that are located in the region of four specific wavelengths such as 850, 1060, 1250, and 1550 nm normally experience an attenuation of less than 0.2 dB/km. It is worth noting that the 850- and 1550-nm transmission windows coincide with the standard transmission windows of fiber communication systems. For this reason, majority of commercial OWC systems operate at these two windows in order to encourage the use of the available off-the-shelf components. Also, wavelengths like 10 μm and ultraviolet (UV) have also been considered for OWC systems. The 10-μm wavelength has better fog transmission characteristics, whereas the UV wavelength is more robust against impairment such as pointing errors and beam blockage. Also, the UV wavelength is less susceptible to solar and other background interferences [8].

Furthermore, it is worth noting that 1520–1600-nm wavelengths are compatible with erbium-doped fiber amplifier (EDFA) technology. This is highly essential in order to achieve high-power and high-data rate systems. Moreover, 1520–1600-nm wavelengths enable transmission of about 50–65 times more average output power than can be transmitted at 780–850 nm for a
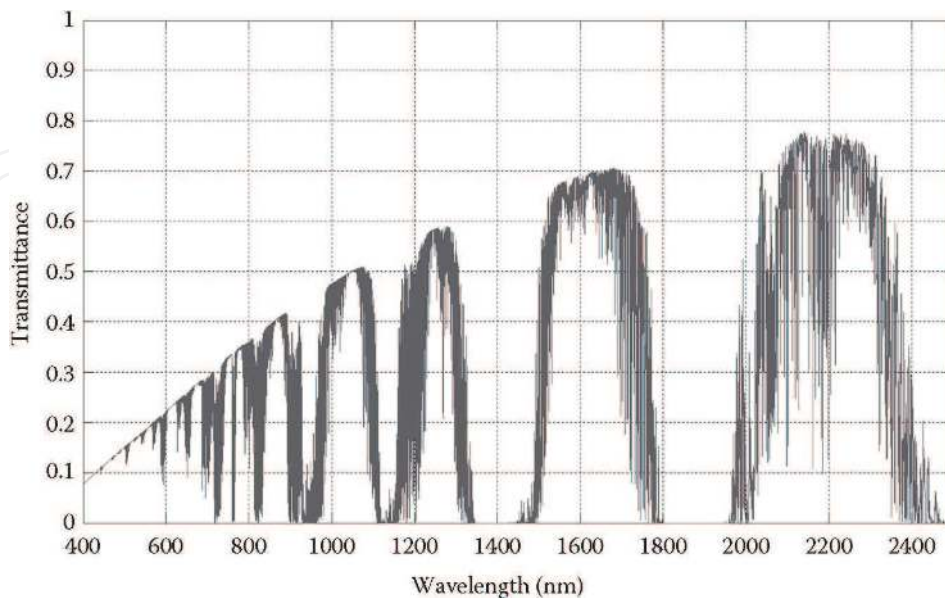
Figure 2. Atmospheric transmittance window with absorption contribution (adapted from Ref. [7]).

specified eye safety classification. This can be attributed to the low transmission of the human eye at these wavelengths [9].

1.2. Safety and regulations

One of the key factors for laser transmitter design is the safety issue. The infrared (IR) light sources can be likely safety threats to human if they are operated inappropriately. Also, exposure to certain optical beams may injure human skin and eye. However, the likely harm to the eye is comparatively more severe due to the eyes' ability to focus and concentrate optical energy. For instance, the eye can focus wavelength range of 0.4–1.4 µm on the retina with enough intensity to damage it; however, other wavelengths can to be absorbed by the front part of the eye before being focused on the retina. It should be noted that laser that is deemed to be "eye-safe" is also "skin-safe" [5, 9].

Moreover, it has been shown that the absorption coefficient at the front part of the eye is considerably greater for longer wavelengths (>1400 nm). Consequently, the permissible average transmission power for lasers operating at 1550 nm is relatively higher. Therefore, they are usually employed for longer transmission range [5, 9].

Figure 3 depicts the absorption of the eye at different wavelengths. At 700–1000-nm spectral range, the cost of optical sources and detectors are relatively low; however, the eye safety regulations are mainly strict. The maximum permissible exposure (MPE) at 900 nm wavelength is ~143 mW/sr. On the other hand, at longer wavelengths (≥1500 nm), the eye safety regulations are relatively less stringent; however, devices operating in these wavelengths are comparatively expensive. The guidelines on the safety of optical beams have been specified by several international standard organizations such as [5, 9]
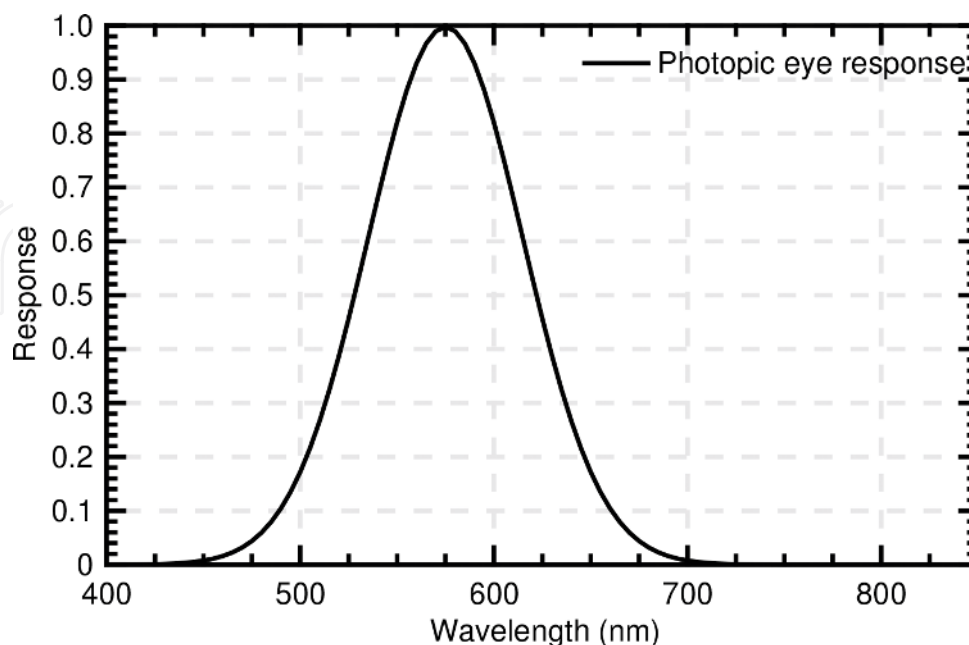

Figure 3. Response of the human eye at different wavelengths.

1. International Electrotechnical Commission (IEC)

2. Center for Devices and Radiological Health (CDRH)

3. European Committee for Electrotechnical Standardization (CENELEC)

4. American National Standards Institute (ANSI)

5. Laser Institute of America (LIA)

The aforementioned organizations have established mechanisms for categorizing lasers in accordance with their type and power. Generally, the classification is based on four groups which are Class 1 through Class 4. Comparatively, Class 1 is the least powerful whereas Class 4 is the most powerful. Also, each of the classes is specified by the accessible emission limits (AELs) metric. The AEL is determined by the optical source wavelength, the emitter geometry, and the source intensity [5, 9]. Consequently, the AEL varies from one OWC category to another. In the subsequent section, we present the major OWC categories.

2. OWC system classification

There have been growing research interests in the OWC system as a viable solution to attend to the NGN requirements in cost-effective ways. The two generic groups of OWC are indoor and outdoor optical wireless communications. The unlimited bandwidth offered by the OWC can be attributed to different bands such as IR, visible (VL), and UV being employed for communication purposes. **Figure 4** shows the electromagnetic spectrum for different applications. Furthermore, the spectrum illustrates the frequency and wavelength ranges being occupied by the bands in OWC. The indoor OWC employs IR or VL light for an in-building wireless solution. It is of high importance especially in scenarios in which the probability of offering network connectivity through physical wired connections is challenging. Moreover, the indoor OWC systems can be categorized into four broad configurations such as tracked, diffused, nondirected LOS, and directed line of sight (LOS). Furthermore, the outdoor OWC employs optical carrier for transporting information from one point to another over an unguided channel that could be an atmosphere or a free space. So, this OWC technology is also known as a free-space optical (FSO) communication system. The FSO communication systems operate
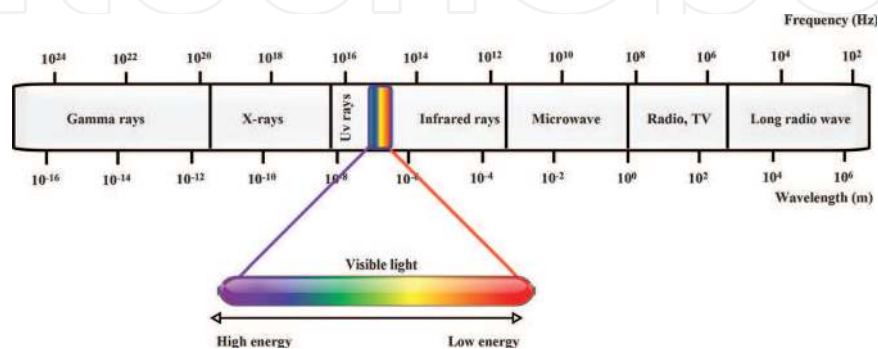

Figure 4. Electromagnetic spectrum.

at the near IR frequencies and are classified into terrestrial and space optical links. These consist of building-to-building, satellite-to-ground, ground-to-satellite, satellite-to-satellite, and satellite-to-airborne platforms (unmanned aerial vehicles [UAVs] or balloons) [10]. The tree diagram in **Figure 5** shows the OWC system classification.

2.1. Underwater optical wireless communications (UOWCs)

The underwater wireless communications are a process of transmitting data in unguided water environments via wireless carriers such as acoustic wave, RF wave, and optical wave. Compared to the RF or acoustic alternatives, UOWC offers higher data rate and transmission bandwidth. Basically, the UOWC uses optical wave as wireless carrier for an unguided data transmission. The UOWC systems are applicable in disaster precaution, offshore exploration, environmental monitoring, as well as military operations. Nevertheless, UOWC systems are susceptible to absorption and scattering which are normally created by the underwater channels. These conditions lead to severe attenuation of optical wave and eventually hindered the system performance. Different viable techniques have been presented in the literature to attend to the associated technical challenges of a UOWC. One of such is an underwater wireless sensor network (UWSN). **Figure 6** depicts a UWSN with aerospace and terrestrial communications.

The major entities in the UWSN are distributed nodes such as relay buoys, seabed sensors, autonomous underwater vehicles (AUVs), and remotely operated underwater vehicles (ROVs). The network entities are capable of performing tasks like processing, sensing, and communication in order to sustain collaborative monitoring of the underwater environment. The acquired data by the sensors that are located at the seabed are transmitted through acoustic/optical links to the AUVs and ROVs which in turn relay the signal to the ships, communication buoys, and other underwater vehicles. Furthermore, the onshore data center that is above the sea surface then processes the data and communicates with the satellite and the ships via RF/FSO links [11].
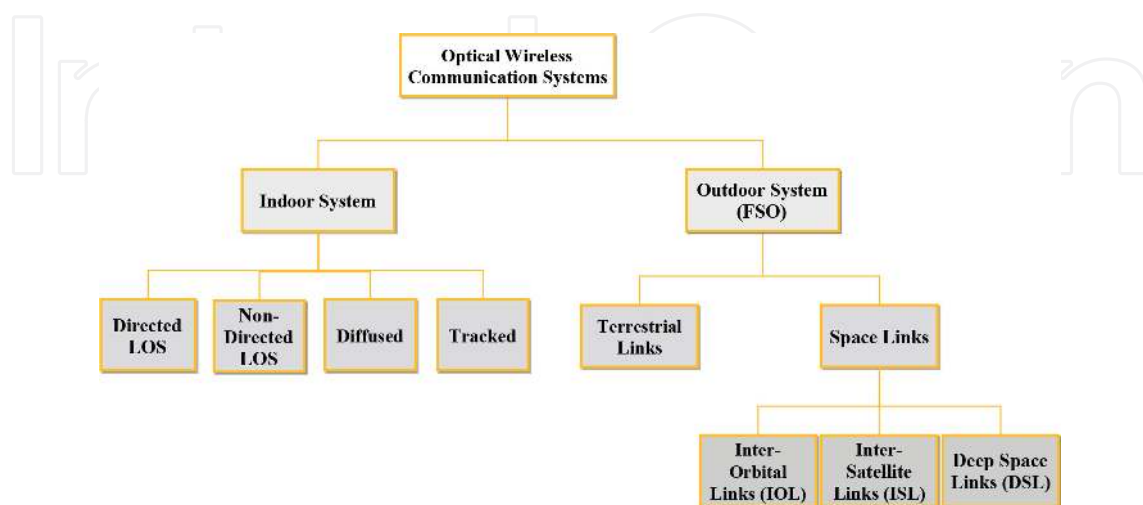
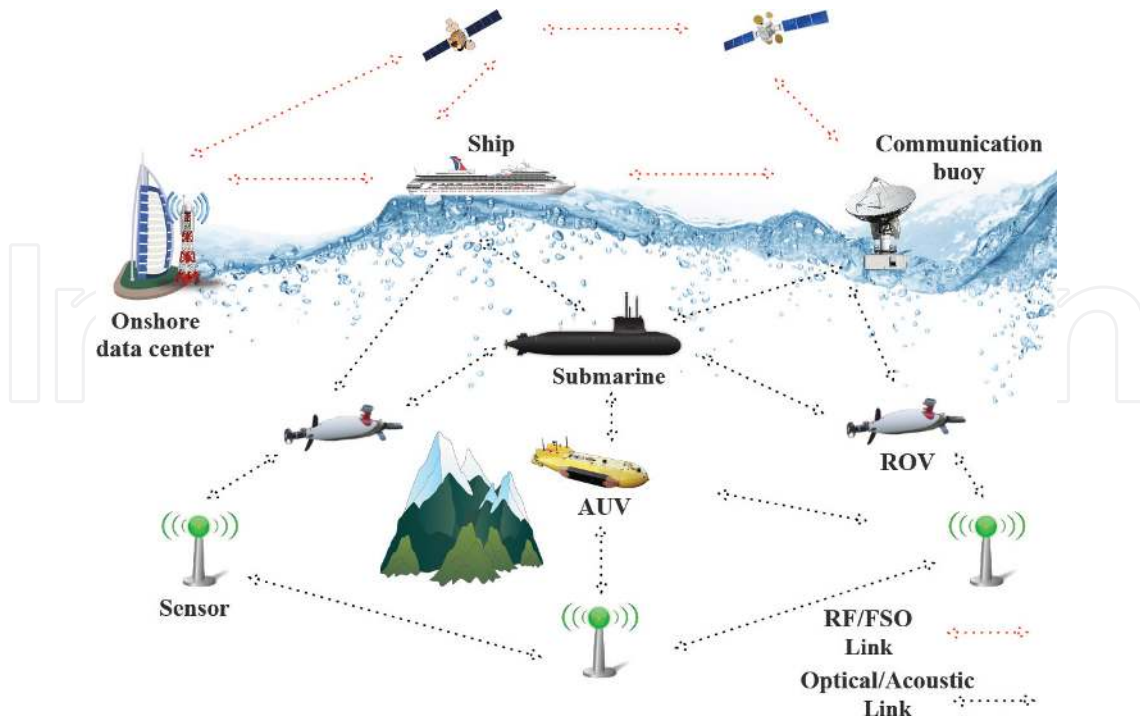**Figure 5.** Optical wireless communication system classification (adapted from Ref. [10]).

Figure 6. UWSN with aerospace and terrestrial communication.

2.1.1. UOWC link configuration

The four categories of UOWC based on the link configurations of the UWSN's nodes are as follows:

1. **Point-to-point line-of-sight (PTP-LOS) configuration**

   The PTP-LOS arrangement is the widely adopted link configuration in the UOWC. In this configuration, the receiver detects the light beam in the direct path to the transmitter. Due to the fact that light sources like lasers are generally used in the PTP-LOS-based systems, precise pointing between the transceiver is essential. Hence, the requirement limits the performance of UOWC systems in turbulent water environments. Also, this can even be more stringent when the transmitter and the receiver of the underwater vehicles are not stationary [11].

2. **Diffused LOS (D-LOS) configuration**

   Unlike the PTP-LOS scheme that employs light sources with narrow divergence angle, the D-LOS is a point-to-multipoint (PTMP) configuration that uses diffused light. The light sources like high-power light-emitting diodes (LEDs) that have large divergence angle are used for the UOWC transmission from one node to multiple nodes. The broadcast nature of this configuration helps in relaxing the requirement for precise pointing. Nonetheless, the scheme is prone to aquatic attenuation which is as a result of the large interaction area with the water. Consequently, this limits D-LOS application to comparatively short distances and lower data rate communications [11].

3. **Retroreflector-based LOS (R-LOS) configuration**

The R-LOS configuration is a special form of PTP-LOS scheme. The R-LOS scheme is appropriate for duplex UOWC systems in which the sensor nodes are expected to have low form factors and consume less power. Due to the fact that there is no laser or other light sources in the retroreflector end, its power consumption, weight, and volume are significantly reduced. However, the R-LOS performance is limited by the backscatter of the transmitted optical signal that may interfere with the reflected signal [11].

4. **Non-line-of-sight (NLOS) configuration**

Another category of UOWC that does not require alignment restriction of LOS is NLOS configuration. The concept of this configuration is that the transmitter launches the beam of light to the sea surface in such a way that the angle of incidence is greater than the critical angle. This ensures that the light beam experiences a total internal reflection. In this scheme, the receiver is directed toward the sea surface in a direction approximately parallel to the reflected light for appropriate signal reception. However, signal dispersion may occur due to the random sea surface slopes (i.e., induced by wind or other turbulence sources) that may reflect the light back to the transmitter [11].

2.1.2. Advantages and challenges of UOWC

The three means of realizing an underwater wireless communication for UWSNs are acoustics, RF, and optics [11]. We compare all schemes so as to point out some salient features and advantages of UOWC:

1. **Acoustic communication**

Acoustic communication is the widely employed method in the underwater wireless communication due to the fact that it is the most viable means of realizing the longest underwater link range. However, the frequency range of operation of acoustic communication is limited (between tens of hertz and hundreds of kilohertz). So, comparatively, this results in low transmission rate in the order of Kbps. Furthermore, the speed of sound wave in the fresh water is about 481 m/s at 2°C and in the salt water it is about 1500 m/s (1500.235 m/s at 1 MPa, 10°C and 3% salinity). These comparative slow propagation speeds make acoustic links prone to serious communication delay. Consequently, acoustic communication cannot be employed in applications that require large volume of data transmission in real time. Additionally, acoustic technology not only impacts marine life but also involves the use of costly, bulky, and energy-consuming transceivers [11].

2. **RF communication**

There are two main advantages of underwater RF communication. In relation to other UWC methods, the RF wave can achieve a smooth transition through the air/water interface. The feature enables a cross-boundary communication that unifies both terrestrial and underwater RF communication systems. It is remarkable that underwater RF communication is the method that is most tolerant to the water turbulence and turbidity. Nevertheless, the method is limited by the associated short link range. Likewise, the

underwater RF methods are cost-ineffective due to the required high energy-consuming transceivers, costly and huge transmission antenna [11].

3. Optical communication

The outstanding technical merits of UOWC are the lowest link delay, highest communication security, highest transmission rate, and lowest implementation costs compared to other methods. The comparative high-speed benefit of UOWC makes it a promising candidate for real-time applications like underwater video transmission. In UOWC systems, LOS configuration is normally employed in the transmission. This helps in preventing eavesdroppers, and hence improves communication security. Besides, UOWC is the most cost-effective and energy efficient means of underwater wireless communication. This can be attributed to the comparatively small, low-energy consuming, and low-cost optical transceivers which are normally employed. This aids in system scalability and large-scale commercialization of UOWC [11]. However, UOWC also has certain associated challenges, which makes its realization highly demanding. The key challenges of UOWC are enumerated as follows:

a.   Poor system performance

When light propagates in water, the photon interacts with the water molecules as well as other particulate matters inside the water. The interaction results in absorption and scattering which attenuate the transmitted optical signal and eventually bring about multipath fading. Consequently, in turbid water environment, UOWC experiences poor BER performance over just a few hundred meters link distance. Furthermore, the presence of matters like chlorophyll and other colored dissolved organic material (CDOM) leads to an increase in the turbidity of the water. So, they reduce the propagation distance of the transmitted optical signal. Besides, since the concentration of CDOM varies with ocean depth variations, the associated light attenuation coefficients also change. This anomaly results in an increase in the system complexity [11, 12].

b.   Intermittent connection

In practice, owing to the narrow divergence feature of blue/green lasers or LEDs, they are usually employed as the light sources in UOWC systems. Therefore, the narrow feature demands a precise alignment between the optical transceivers. However, there is high tendency for intermittent misalignment of optical transceivers because of the turbulence in the underwater environment. Hence, sporadic movements of the sea surface will bring about severe connectivity loss [11, 12].

c.   Energy constraint and system reliability

Factors such as the pressure, temperature, flow, and salinity of the seawater have high impact on the performance and lifetime of UOWC devices. Furthermore, UOWC devices are susceptible to failures due to corrosion and fouling. So, reliable underwater devices are required for effective communications. Also, due to the fact that exploitation of solar energy is extremely difficult and UOWC devices are expected to

experience extended operation time, then, reliability of the batteries and power consumption efficiency of device are essential in a UOWC environment [11, 12].
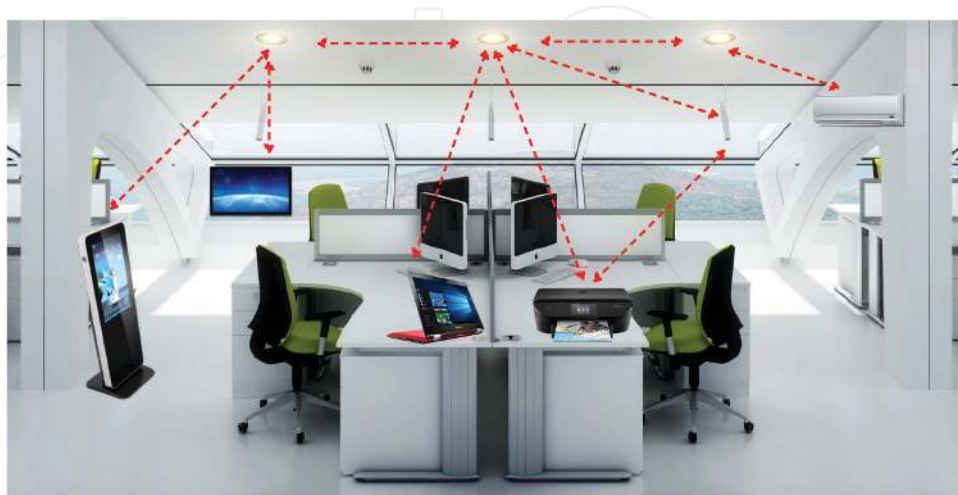
2.2. Visible light communication (VLC) systems

The current enhancement of LED chip design with swift nanosecond-switching times and extensive deployment of LEDs for energy efficiency paves the way for visible light communication (VLC) system [13, 14]. So, the VLC system has become an attractive technology for addressing challenges such as energy efficiency, bandwidth limitation, electromagnetic radiation, and safety in wireless communications [15, 16]. The VLC system operates in the wavelength range of ~390–750 nm. **Table 1** shows the seven colors with specific frequency and wavelength for visible spectrum. **Figure 7** illustrates VLC system implementation. The concurrent support for communication and illumination by the VLC offers the following advantages over the RF communications.

Color	Wavelength (nm)	Frequency (THz)
Violet	440–405	680–740
Indigo	455–440	660–680
Blue	475–455	630–660
Green	560–475	535–630
Yellow	585–560	515–535
Orange	605–585	495–515
Red	685–605	435–495

Adapted from Ref. [17].

Table 1. Visible spectrum colors.

Figure 7. Visible light communication system.

2.2.1. Huge bandwidth

It exhibit almost unlimited and unlicensed bandwidth which approximately ranges from 380 to 780 nm. Therefore, VLC has 350 THz that can support multi-gigabit-per-second data rates with LED arrays in a multiple-input multiple-output (MIMO) configuration [14]. This makes VLC a good alternative to the indoor IR that operates at 780–950 nm for the access technologies [6].

2.2.2. Low power consumption

VLC provides both communication and lighting, giving Gbps data rates with only unsophisticated LEDs and photodetectors (PDs) that consume low power compared to costly RF alternatives that demand high power consumption for sampling, processing, and transmitting Gbps data [14].

2.2.3. Low cost

The required optical components such as LEDs and photodetectors are inexpensive, compact, lightweight, amenable to dense integration, and have very long lifespan [13]. Moreover, with large unlicensed optical spectrum as well as much lower power-per-bit cost compared to the RF communications, VLC is relatively cheaper.

2.2.4. No health concerns

VLC does not generate radiation that leads to public health concern. Besides, it lowers the carbon dioxide emission owing to the little extra power consumption for communication purposes [18].

2.2.5. Ubiquitous computing

Due to the fact that there are various luminous devices like traffic signs, commercial displays, indoor/outdoor lamps, TVs, car headlights/taillights, and so on being used everywhere, VLC can be employed for a wide range of network connectivity [19].

2.2.6. Inherent security

VLC offers comparatively higher security due to the fact that it is highly intricate for a network intruder that is outside to pick up the signal [14].

2.2.7. Indoor localization

The existing RF-based global positioning system (GPS) gives inadequate or no network coverage in the indoor and underground (e.g., tunnel) environment. This is as a result of high attenuation, multipath, and the safety regulation. These factors lead to an accuracy of only up to a few meters for the RF-based GPS. The VLC-based indoor positioning can be employed to attend to the issues in the enclosed environments. So, the VLC-based indoor navigation services offer very high accuracy to within a few centimeters. In essence, VLC offers good

indoor localization system using the white LEDs. Furthermore, LEDs give better light source that is more than 400 lux. This is sufficient for high-speed data transmission compared to the incandescent and fluorescent sources. Moreover, LEDs have longer lifespan that results in ecological and financial benefits [6].

In addition, VLC is an alternative technology in sensitive or hazardous environments like airplanes, hospitals, and industrial gas production plants where the employment of RF technology is not permitted. The worldwide research community through bodies like the Wireless World Research Forum, the IEEE standardization body, the VLC consortium, the UK research council, and the European OMEGA project has embraced the indoor short-range VLC as a promising scheme because of the associated excellent attributes [6].

However, simultaneous employment of light sources for the data communication as well as illumination causes certain challenges that require consideration for VLC system implementations to be viable. Flicker mitigation and dimming support are the two major challenges of visible light spectrum [14, 20]. In the contemporary lighting systems, the light sources are equipped with dimming control functionality that enables the users to control the average brightness of light sources to their preferred level. Flicker is the variation in the brightness of light perceived by the human naked eye. Flicker is as a result of continuous switching on and off of the light source during data transmission. It is essential to mitigate any possible flicker because it can instigate negative/harmful physiological changes in humans. Flicker can be prevented by making the changes in brightness be within the maximum flickering time period (MFTP). The MFTP is the maximum time period within which the light intensity can be changed without any perception by the human eye [14]. Also, various modulation formats have been recommended for VLC in view of dimming control and flicker mitigation. For instance, the IEEE 802.15.7 standard proposes variable pulse position modulation (VPPM) for VLC system because of its notable ability to control dimming. It integrates the pulse position modulation (PPM) and pulse width modulation (PWM) in order to support communication with dimming control [14, 20]. Furthermore, other challenges are high path losses, multipath-induced intersymbol interference (ISI), artificial light-induced interference, and blocking. Moreover, LED electro-optic response nonlinearity has to be taken into consideration [6].

2.3. Wireless body area network (WBAN)

Wireless body area network (WBAN) is a system that comprises a set of miniaturized low-power, lightweight sensor nodes, which form wireless sensor networks (WSNs). **Figure 8** shows a WBAN system for medical monitoring. With the help of the sensor nodes, WBANs have emerged as an attractive alternative to the conventional wired medical network. Also, there has been noteworthy increase in the WBAN systems because of the IEEE 802.15.6 standard that regulates their commercial applications. Furthermore, there is an obligation on 2.36–2.40-GHz frequency band as a medical-only WBAN band by the Federal Communications Commission (FCC). The restriction is purposely for service provisions for the indoor health-care facilities as well as for supporting the patients' health-care information and management [21, 22]. Furthermore, the constraint is also to guarantee high quality of service for the health information transmission.
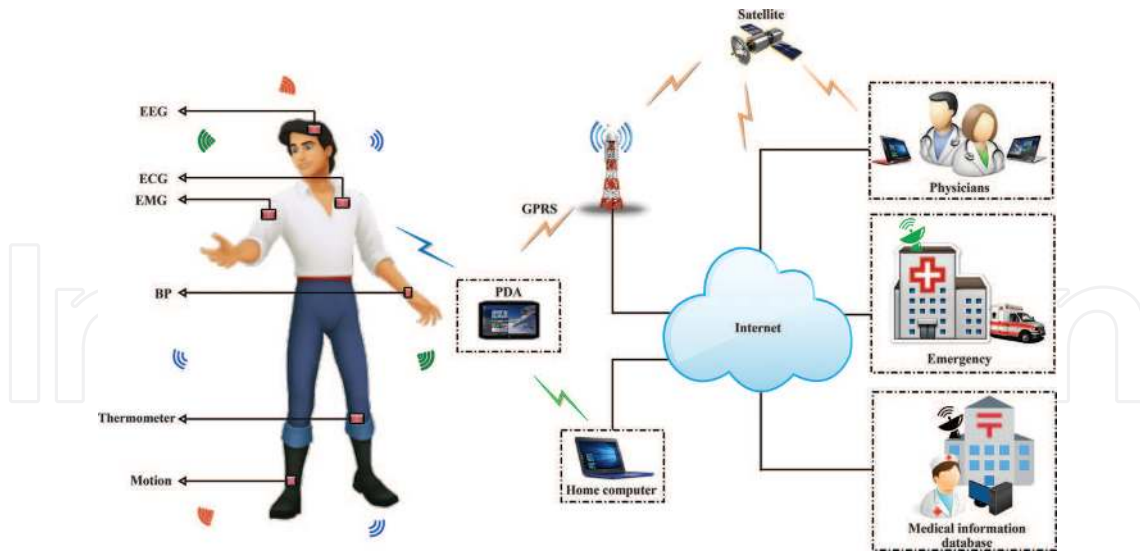
Figure 8. Wireless body area network.

The distributed sensors in the WBAN can be implanted in or on the human body in order to monitor physiological parameters in real time. The implanted sensors that are wirelessly connected to the outside network through a central unit collect different vital health information. The monitored physiological data include electromyogram (EMG), electroencephalogram (EEG), electrocardiogram (ECG), temperature, heart rate, blood pressure (BP), and glucose level [22]. The ZigBee, Bluetooth, as well as the current Bluetooth Low Energy (BLE) are contending for market share of wireless health devices. Their major appealing advantages are low power consumption and the added mobility [23]. Health devices that employ these technologies are operating in the industrial, scientific, and medical (ISM) radio bands. High emissions from these devices can create electromagnetic interference (EMI) and eventually disrupt communication. Similarly, there are security issues concerning data transmission for patient monitoring which are susceptible to hacking [23].

Furthermore, it should be noted that the existing WBANs that use ultra-wide band (UWB) transmissions are RF based. However, their implementation in the hospitals and medical facilities where RF-based system deployment is restricted or prohibited can be challenging. This is due to the potential effects of EMI from various RF transceivers on medical devices. The EMI effects can lead to medical equipment malfunction. Also, RF wave propagation on and/or in the human body is highly complex to examine. Consequently, to address these challenges OWC can be employed as an alternative solution [24].

The ECG signal and patient information can be transmitted concurrently with the help of VLC technology. Moreover, certain medical equipment like the one for the cardiac stress test (or cardiac diagnostic test) can be improved on by incorporating LEDs on the sensor units. This implementation will help in minimizing the large amount of cables (e.g., electrodes) that are normally required. Besides, VLC employment is greener (green communication and networking), safer, more secure in RF-restricted/prohibited hospitals and medical facilities [23]. Furthermore, it is worth noting that the current advancements in the organic LED (OLED) technology enable the integration of VLC transceivers into wearable gadgets and clothing [24].

2.4. Optical space communications

An effective communication links between satellites enable better flexibility, extended coverage, and improved connectivity to be achieved in satellite systems. This is applicable in interorbit links between satellites in low earth orbit (LEO) and geostationary orbit (GEO). Furthermore, intersatellite links between satellites in the same GEO or LEO orbit are other scenarios for application. Also, the satellite system connectivity can be enhanced by exploiting the free-space links between satellites. This will result in an improved capacity for telecommunication systems. Moreover, the capability to relay data from the earth observation satellite to the ground through a GEO relay satellite enables real-time data flow and minimizes the number of ground stations required for service delivery in the system [25].

Generally, the space link implementation can be realized at microwave, millimetric, and optical frequencies. Also, all technologies require the communication beam that emanates from the transmitting terminal to be pointed toward the receiving terminal with sufficient accuracy. This is necessary in order to meet the required link power budget. **Table 2** presents typical antenna gains and beamwidths for intersatellite link technologies [25].

It should be noted that out of the technologies, optical frequency offers an exceptionally high antenna gain for comparatively small antenna size. Therefore, optical links provide significant advantages such as low mass, low power consumption, and reduced size. As demonstrated in [26], the optical antenna diameter may be relatively smaller than that of RF by a factor of 13. Also, its mass and power can be half of that for RF systems. **Table 3** compares different communication technologies in terms of mass, power, and antenna diameter. An architecture that depicts ground-to-satellite optical links that are connected to satellite network and then satellite-to-ground optical links is illustrated in **Figure 9**. The salient features of optical links enable small terminals that can be easily accommodated on the satellite [25]. Also, optical space-based communication offers high-data rate, large capacity, minimized interference risk with other communication systems, and efficient utilization of frequency resources [10, 26].

Nevertheless, the space FSO communications are susceptible to atmospheric effects which make the channel a random function of space and time. Consequently, the uplink/downlink transmissions suffer from losses such as atmospheric scintillation, beam divergence, absorption, scattering, misalignment, cloud blockage, background noise and angle-of-arrival fluctuations. It should be noted that the losses confronted by the beam in the FSO uplink transmission

| Band	Parameters			
	Frequency	Antenna diameter (m)	Antenna gain (dBi)	3 dB beamwidth degrees
S-band	2 GHz	2	30	5.25
Ka-band	26 GHz	2	52	0.40
Millimeter	60 GHz	1	53	0.35
Optical	0.36 PHz	0.07	108	6.7×10^{-4}

Adapted from Ref. [25].

Table 2. Intersatellite link technologies comparison.

Link	Frequency band								
	Optical			*Ka*			Millimeter		
	Antenna diameter	Mass	Power	Antenna diameter	Mass	Power	Antenna diameter	Mass	Power
GEO-LEO	10.2 cm (1.0)	65.3 kg (1.0)	93.8 W (1.0)	2.2 m (21.6)	152.8 kg (2.3)	213.9 W (2.3)	1.9 m (18.6)	131.9 kg (2.0)	184.7 W (2.0)
GEO-GEO	13.5 cm (1.0)	86.4 kg (1.0)	124.2 W (1.0)	2.1 m (15.6)	145.8 kg (1.7)	204.2 W (1.6)	1.8 m (13.3)	125.0 kg (1.4)	175.0 W (1.4)
LEO-LEO	3.6 cm (1.0)	23.0 kg (1.0)	33.1 W (1.0)	0.8 m (22.2)	55.6 kg (2.4)	77.8 W (2.3)	0.7 m (19.4)	48.6 kg (2.1)	68.1 W (2.1)

Adapted from Ref. [26].

Table 3. Comparison of different technologies with transmit power of 10, 50, and 20 W for optical-, Ka-, and millimeter-band systems, respectively.
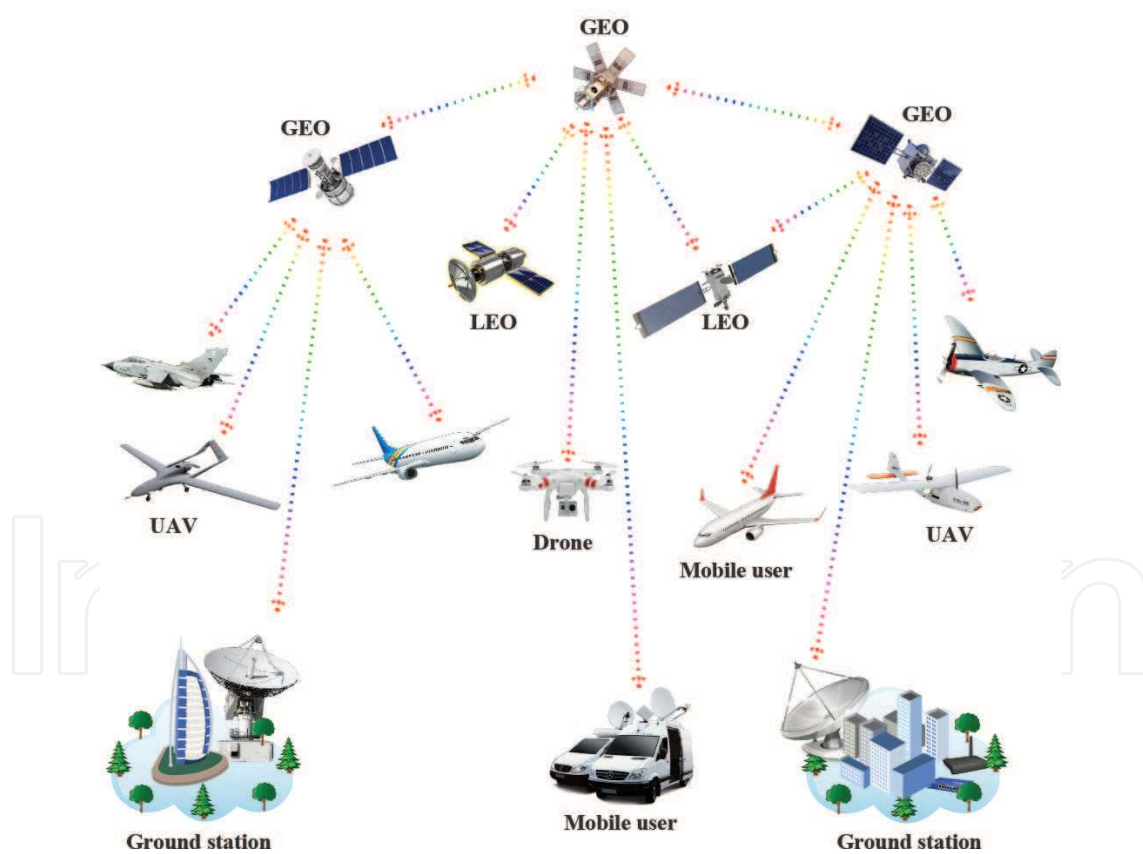

Figure 9. Space optical communication.

are very large compared to downlink transmission. Furthermore, the intersatellite FSO links are insusceptible to weather conditions due to the fact that the satellite orbits are at a considerable distance over the atmosphere [10]. However, the associated narrow optical beamwidths

bring about stringent pointing, acquisition, and tracking (PAT) requirements for optical systems. This can also be attributed to different relative velocity of the satellite. So, a compact low-mass PAT system is required to address PAT requirements [26].

2.5. Terrestrial free-space optical (FSO) communications

There have been much more research effort in terrestrial FSO partly because of some successful field trials and commercial deployments [27–31]. **Figure 10** shows a scenario for FSO system deployment as a universal platform for a nippy as well as an efficient ubiquitous wireless service provision for the future broadband access networks. The significant attentions being attracted by the FSO systems are primarily due to their inherent advantages such as cost-effectiveness, lower power consumption (high-energy-efficiency-green communication), ease of deployment, higher bandwidth/capacity, more compact/low-mass equipment, reduced time-to-market, immunity to EMI, high degree of security against eavesdropping, license-free operation, as well as better protection against interferences, compared with the traditional RF communication systems [32, 33]. These salient features make FSO communication systems very appealing for a variety of applications in disaster recovery, radio astronomy, remote-
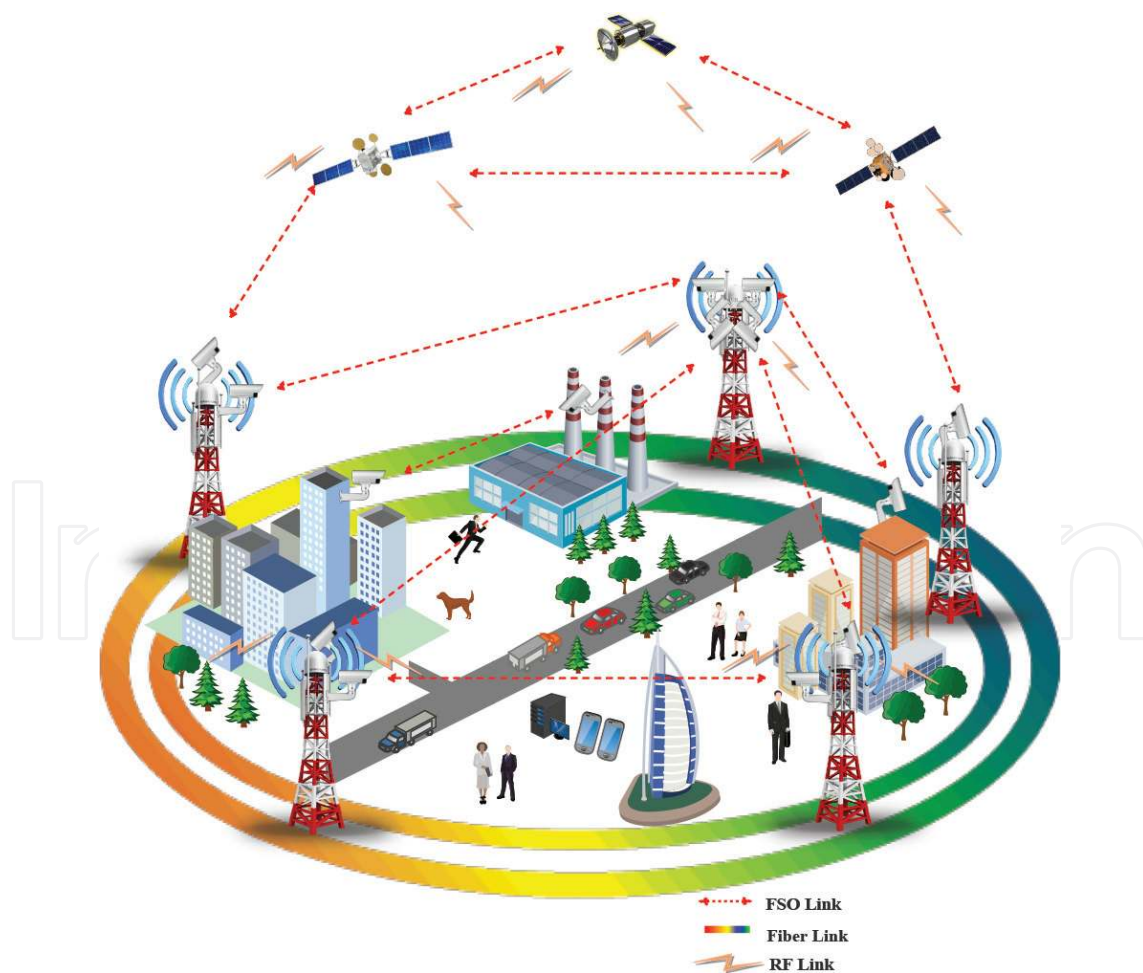
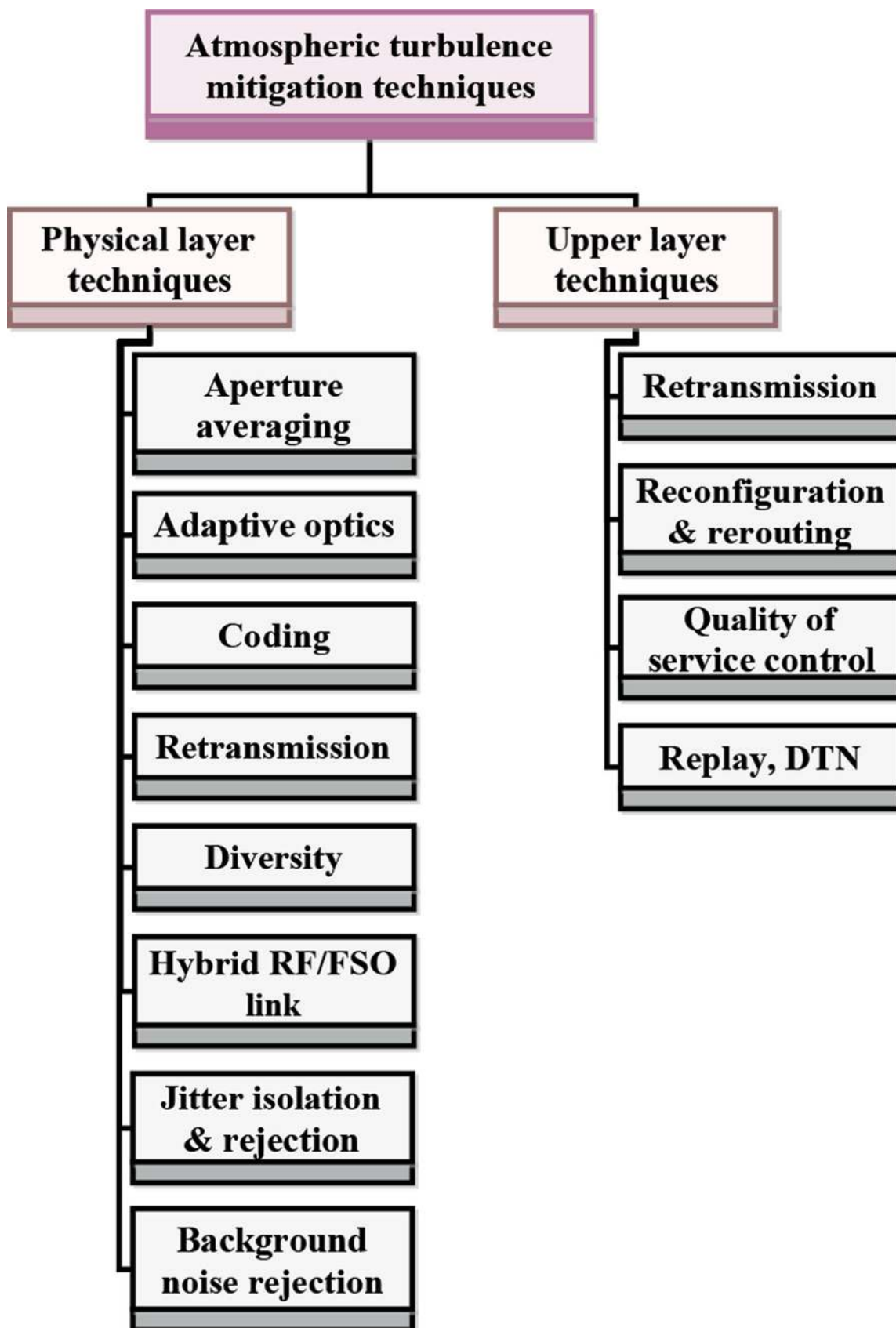**Figure 10.** A scenario for OWC system deployment for access networks.

Figure 11. Atmospheric turbulence mitigation techniques (adapted from Ref. [10]).

sensing/surveillance/monitoring, metropolitan area network extension, high-definition TV transmission, sharing of medical imaging in real time, and fronthaul and backhaul for wireless cellular networks [3, 8]. Moreover, apart from being used for establishing terrestrial links, they are applicable for launching high-speed interplanetary space links such as intersatellite/deep space and ground-to-satellite/satellite-to-ground links [10].

In spite of the advantages of FSO communication and diverse application, its extensive use is hindered by some challenges in real-life scenarios. For instance, the FSO links are susceptible to scattering caused by adverse weather conditions like snow, rain, and fog [8, 33]. Moreover, building sway caused by factors such as thermal expansion, wind loads, and weak earthquakes also impairs the FSO link performance [33]. Also, atmospheric turbulence-induced fading has been recognized as the main contributor of the FSO link impairment [33, 34]. Consequently, the system performance is impeded as a result of atmospheric effects which cause loss of spatial coherence, beam spreading, and temporal irradiance fluctuation known as scintillation or fading [8, 35]. Scintillation manifests as temporal and spatial variation in the light intensity along the transmission path. This is due to the random changes in the refractive index which is as a result of the inhomogeneities in the air temperature and pressure [8, 32]. For these reasons, the dispersive nature of the link needs considerable attention when modeling an FSO system. This will help in supporting the stringent requirements of various bandwidth-intensive mobile applications of the NGNs [3]. The FSO link impairment modelings are discussed in Section 3. The tree diagram in **Figure 11** presents different atmospheric turbulence mitigation techniques.

3. Optical system and channel model

Assuming a practical FSO link with intensity-modulation/direct-detection (IM/DD) using OOK modulation, the data are modulated onto the instantaneous intensity of an optical beam at the transmitter. The optical power emanated from the transmit aperture into the free space is assumed to be affected by factors such as misalignment fading (pointing errors), atmospheric turbulence-induced fading, and background noise or ambient noise before reaching the receive aperture. These factors lead to the signal intensity fluctuation. Consequently, the subsequent received electrical signal, r, at the receive aperture can be modeled as [3, 35–37]

$$r = \eta_e h x + n, \tag{1}$$

where $x \in \{0,1\}$ denotes the transmitted information bit, η_e is the effective photoelectric conversion ratio of the receiver, n is additive white Gaussian noise (AWGN) with zero mean and variance, $\sigma_n^2 = N_0/2, N_0$ is a one-sided noise power spectral density in watts/Hz, and $h = h_\ell h_a h_p$ represents the irradiance that influences the channel state. The channel irradiance in Eq. (1) is a product of the deterministic path loss, h_ℓ: the random attenuation (i.e., atmospheric turbulence-induced fading), h_a, as well as the random attenuation (due to geometric spread and pointing errors), h_p. The h_a and h_p are random variables with probability density functions (pdfs) $f_{h_a}(h_a)$ and $f_{h_p}(h_p)$, respectively.

3.1. Atmospheric attenuation

When an optical beam passes through the atmosphere, it experiences atmospheric loss. The attenuation suffered by the signal power according to the exponential Beers-Lambert law is given by [36–38]

$$h_\ell(\lambda, z) = \frac{P(\lambda, z)}{P(\lambda, 0)} = \exp\left(-\sigma(\lambda)z\right) \tag{2}$$

where $h_\ell(\lambda, z)$ denotes the loss that is a function of propagation path of length z at wavelength λ, $P(\lambda, z)$ and $P(\lambda, 0)$ are the signal power and the emitted power at distance z, respectively. The attenuation coefficient or the total extinction coefficient, $\sigma(\lambda)$ per unit of length, is given by [36]

$$\sigma(\lambda) = \alpha_m(\lambda) + \alpha_a(\lambda) + \beta_m(\lambda) + \beta_a(\lambda), \tag{3}$$

where $\alpha_{m,a}$ represent molecular and aerosol absorption coefficients, respectively, and $\beta_{m,a}$ denote molecular and aerosol scattering coefficients, respectively.

The attenuation h_ℓ is assumed to be a constant scaling factor over a long time period, so, there is no haphazard behavior. Moreover, it is subject to the distribution and size of the scattering particles as well as the wavelength employed. It can be expressed in terms of visibility, which can be measured directly from the atmosphere. Empirically, attenuation can be defined in terms of visibility as [36]

$$\sigma(\lambda) = \frac{3.912}{V} \left(\frac{\lambda}{550}\right)^{-q}, \tag{4}$$

where V is the visibility (in kilometers) and q is a parameter that depends on the particle size distribution in the atmosphere expressed by the Kruse model as [36]

$$q = \begin{cases} 1.6 & V > 50\,\text{km} \\ 1.3 & 6\,\text{km} < V < 50\,\text{km} \\ 0.585V^{1/3} & V < 6\,\text{km} \end{cases} \tag{5}$$

Furthermore, Kim presents an extended model in order to achieve a better accuracy at lower visibility scenarios. The Kim model is expressed as [36]

$$q = \begin{cases} 1.6 & V > 50\,\text{km} \\ 1.3 & 6\,\text{km} < V < 50\,\text{km} \\ 0.16V + 0.34 & 1\,\text{km} < V < 6\,\text{km} \\ V - 0.5 & 0.5\,\text{km} < V < 1\,\text{km} \\ 0 & V < 0.5\,\text{km} \end{cases} \tag{6}$$

3.2. Pointing error or misalignment fading

An FSO link is an LOS communication with narrow optical beamwidth that brings stringent pointing accuracy requirements for efficient performance and reliability of optical systems.

Pointing errors and signal fading normally occur at the receiver because of the wind loads and thermal expansions that lead to random building sways. Assuming a Gaussian spatial intensity profile of beam waist w_z at the receiver plane, located at distance z away from the transmitter. Also, suppose a circular aperture of radius r, the collected power fraction owing to the geometric spread with radial displacement α, from the detector origin can be approximated as the Gaussian form [37, 38]

$$h_{\mathrm{p}}(\alpha) \approx A_0 \exp\left(-\frac{2\alpha^2}{w_{z_{eq}}^2}\right) \tag{7}$$

where $w_{z_{eq}}^2 = w_z^2 \sqrt{\pi}\,\mathrm{erf}(v)/2v \exp(-v^2)$, $v = \sqrt{\pi}r/\sqrt{2}w_z$, $A_0 = [\mathrm{erf}(v)]^2$, $w_{z_{eq}}$ is the equivalent beamwidth, and $\mathrm{erf}(\cdot)$ denotes the error function given by [39]

$$\mathrm{erf}(x) = (2/\sqrt{\pi})\int_0^x e^{-u^2}\,du \tag{8}$$

If we assume that the elevation and the horizontal sway are independent and identical Gaussian distributions, then the radial displacement, α, follows a Rayleigh distribution. Then, the $f_{h_{\mathrm{p}}}(h_{\mathrm{p}})$ can be defined as [37, 38]

$$f_{h_{\mathrm{p}}}(h_{\mathrm{p}}) = \frac{\gamma^2}{A_0^{\gamma^2}} h_{\mathrm{p}}^{\gamma^2 - 1}, \quad 0 \leq h_{\mathrm{p}} \leq A_0 \tag{9}$$

where $\gamma = w_{z_{eq}}/2\sigma_s$ represents the ratio between the equivalent beam radius and the standard deviation (jitter) of the pointing error displacement at the receiver and σ_s^2 is the jitter variance at the receiver.

3.3. Atmospheric turbulence

The intensity fluctuation over the FSO channel has been defined by several statistical models in the literature for different turbulence regimes. One of such model is the log-normal (LN) distribution that has been extensively employed because of its significant match with the experimental measurements. This is discussed further in Section 6. Some of other widely employed models are gamma-gamma ($\Gamma\Gamma$), negative exponential, K distribution, and I-K distribution. However, in this work, we focus on the LN, $\Gamma\Gamma$, and generic Málaga (M)-distribution models.

3.3.1. Log-normal distribution (LN)

In general, the LN model is only suitable for weak turbulence conditions and for link range that is less than 100 m [40]. So, the intensity fluctuation pdf for the weak turbulence modeled by the LN distribution is given by [3, 35]

$$f_{h_a}(h_a) = \frac{1}{2h_a\sqrt{2\pi\sigma_x^2}} \exp\left(-\frac{(\ln(h_a) + 2\sigma_x)^2}{8\sigma_x^2}\right), \tag{10}$$

where $\sigma_x^2 = \sigma_l^2/4$ represents the log-amplitude variance defined for plane wave and spherical waves, respectively as [3, 35]

$$\sigma_x^2|_{\text{plane}} = 0.307 C_n^2 k^{7/6} L^{11/6}, \tag{11}$$

$$\sigma_x^2|_{\text{spherical}} = 0.124 C_n^2 k^{7/6} L^{11/6}, \tag{12}$$

$$\sigma_l^2|_{\text{plane}} = 1.23 C_n^2 k^{7/6} L^{11/6}, \tag{13}$$

$$\sigma_l^2|_{\text{spherical}} = 0.50 C_n^2 k^{7/6} L^{11/6}, \tag{14}$$

where σ_l^2 is the log-irradiance variance, $k = 2\pi/\lambda$ represents the optical wave number, L denotes the distance, and C_n^2 is the altitude-dependent index of refraction structure parameter. The C_n^2 is a main parameter for distinguishing the amount of refractive index fluctuation in the atmospheric turbulence. It is a function of the atmospheric altitude, wavelength, and temperature. There are a number of C_n^2 profile models being proposed in the literature; however, the extensively used one in terms of altitude is the Hufnagle-Valley model given by [3, 5, 35, 39]

$$C_n^2(h) = 0.00594(v_w/27)^2 (10^{-5}h)^{10} \exp\left(-h/1000\right) + 2.7 \times 10^{-16} \exp\left(-h/1500\right) + \hat{A} \exp\left(-h/100\right), \tag{15}$$

where h signifies the altitude in meters (m) and $\hat{A}$ represents the nominal value of $C_n^2(0)$ at the ground level in $m^{-2/3}$. The value of C_n^2 for the FSO links near the ground level is approximately $1.7 \times 10^{-14} m^{-2/3}$ and $8.4 \times 10^{-14} m^{-2/3}$ during the daytime and at the night, respectively. Generally, C_n^2 ranges from $10^{-13} m^{-2/3}$ for the strong turbulence to $10^{-17} m^{-2/3}$ for the weak turbulence. Its typical average value is $10^{-15} m^{-2/3}$ [5, 39]. The v_w denotes the root mean square (rms) wind speed (pseudowind) in meters per second (m/s) with the most usual value of 21 m/s, but it can be described by [39]

$$w = \left[\frac{1}{15 \times 10^3} \int_{5\times10^3}^{20\times10^3} V^2(h)dh\right]^{1/2}, \tag{16}$$

where $V(h)$ is normally defined by the Bufton wind model that can be expressed as [39]

$$V(h) = \omega_s h + V_g + 30\exp\left[-\left(\frac{h - 9400}{4800}\right)^2\right] \tag{17}$$

where V_g denotes the ground wind speed and ω_s signifies the *slew rate* that is related to the satellite movement regarding the observer on the ground.
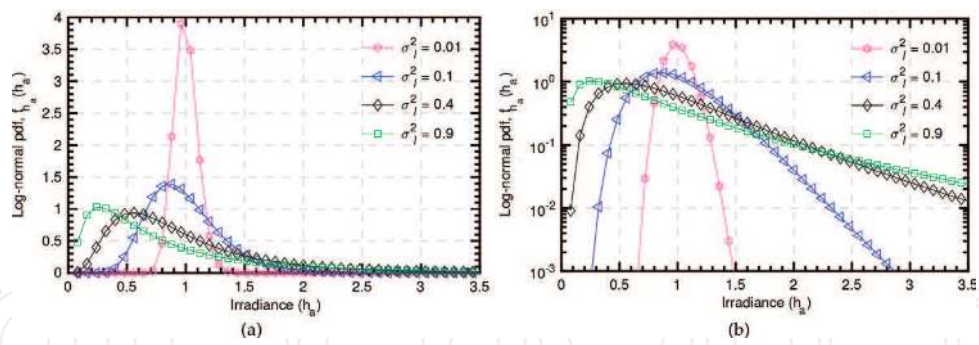
Figure 12. Log-normal pdf for different values of log-irradiance variance using (a) linear scale and (b) logarithmic scale.

We substitute different values of the log-irradiance variance, that is, $\sigma_l^2 \in$ (0.01, 0.1, 0.4, 0.9) in Eq. (11) into Eq. (10) in order to estimate the intensity fluctuation pdf for the LN distribution. The LN pdf plot can be easily achieved by using a linear scale; however, we also present results of a logarithmic scale implementation. This is to ensure uniformity in this chapter because we are going to use the logarithmic scale to present experimental results of irradiance fluctuation in Section 6. Moreover, logarithmic scale has the ability to respond to skewness toward the large values. So, it is more appropriate for illustrating how the measured samples would fit with the distributions at their tails. **Figure 12** shows the LN pdf for different values of log-irradiance variance. In **Figure 12a**, linear scale is employed whereas in **Figure 12b** we use logarithmic scale. It is crystal clear that detailed insight of the tails of the plots is presented in **Figure 12b**. Furthermore, it should be noted that as the value of σ_l^2 increases, the distribution is getting more and more tilted. This signifies the magnitude of the irradiance fluctuation of the system.

3.3.2. Gamma-gamma ($\Gamma\Gamma$) distribution

In most cases, in the strong turbulence regimes in which the LN distribution characterization is not valid, the $\Gamma\Gamma$ distribution is normally employed in modeling the scintillation effects. Also, the $\Gamma\Gamma$ model can be used in characterizing the fading gains from the weak to the strong turbulence scenarios. The pdf of h_a using the $\Gamma\Gamma$ distribution is given by [3, 5, 35, 39]

$$f_{h_a}(h_a) = \frac{2(\alpha\beta)^{(\alpha+\beta)/2}}{\Gamma(\alpha)\Gamma(\beta)}(h_a)^{\frac{(\alpha+\beta)}{2}-1}K_{\alpha-\beta}(2\sqrt{\alpha\beta h_a}), \tag{18}$$

where $\Gamma(\cdot)$ represents the gamma function, $K_\nu(\cdot)$ is the modified Bessel function of the second kind of order ν, α and β are the effective number of large-scale and small-scale eddies of the scattering process, respectively. The parameters α and β are defined, respectively, for the plane wave as [3, 5, 35, 39]

$$\alpha = \left[\exp\left(\frac{0.49\sigma_R^2}{(1+1.11\sigma_R^{12/5})^{7/6}}\right) - 1\right]^{-1}, \tag{19}$$

$$\beta = \left[\exp\left(\frac{0.51\sigma_R^2}{(1+0.69\sigma_R^{12/5})^{5/6}}\right) - 1\right]^{-1}, \tag{20}$$

and for the spherical wave, they can be expressed as [35]

$$\alpha = \left[\exp\left(\frac{0.49\sigma_R^2}{(1 + 0.18d^2 + 0.56\sigma_R^{12/5})^{7/6}} \right) - 1 \right]^{-1}, \tag{21}$$

$$\beta = \left[\exp\left(\frac{0.51\sigma_R^2(1 + 0.69\sigma_R^{12/5})^{-5/6}}{(1 + 0.9d^2 + 0.62d^2\sigma_R^{12/5})^{5/6}} \right) - 1 \right]^{-1}, \tag{22}$$

where $d \triangleq (kD^2/4L)^{1/2}$, D represents the diameter of the receiver aperture, and σ_R^2 denotes the Rytov variance which is a metric for the strength of the turbulence fluctuations. The σ_R^2 is defined for the plane and the spherical waves, respectively, as [5, 35, 39]

$$\sigma_R^2\big|_{\text{plane}} = 1.23 \, C_n^2 \, k^{7/6} \, L^{11/6}, \tag{23}$$

$$\sigma_R^2\big|_{\text{spherical}} = 0.492 \, C_n^2 \, k^{7/6} \, L^{11/6}, \tag{24}$$

Apart from different values of σ_I^2 being employed, that is, $\sigma_I^2 \in (4.0, 1.5, 0.5)$, we substitute different values of the effective number of large- and small-scale eddies of the scattering process, that is, α and $\beta \Rightarrow \alpha \in (4.3, 4.1, 6.0)$ and $\beta \in (1.3, 2.0, 4.4)$ in Eq. (19) and Eq. (20) into Eq. (18) to estimate the $\Gamma\Gamma$ pdf. The results of both linear and logarithmic scales are depicted in **Figure 13**. **Figure 13** shows turbulence regimes that correspond to the weak, moderate, and strong atmospheric scenarios. The results show that an increase in the turbulence from the weak regime to the strong regime leads to corresponding increase in the distribution spreading.

The normalized variance of the irradiance also known as the scintillation index (σ_N^2) can be expressed in terms of σ_x^2 and eddies of the scattering process (α and β), respectively, as [35, 39]

$$\sigma_N^2 \triangleq \frac{\langle h_a^2 \rangle - \langle h_a \rangle^2}{\langle h_a \rangle^2} \tag{25}$$

$$= \frac{\langle h_a^2 \rangle}{\langle h_a \rangle^2} - 1 \tag{26}$$

$$= exp(4\sigma_x^2) - 1 \tag{27}$$

$$= 1/\alpha + 1/\beta + 1/(\alpha\beta). \tag{28}$$

3.3.3. Málaga (𝓜)-distribution

The 𝓜-distribution is a generic model that is appropriate for defining the entire turbulent regimes. **Table 4** shows the means of generating the existing atmospheric turbulence models from the 𝓜-distribution model [41]. The 𝓜-distributed fading model is based on components such as U_L, U_S^C, and U_S^G which represent the line-of-sight (LOS) component, the scattered component by the eddies on the propagation axis that is coupled to the LOS contribution, and the scattered component to the receiver by the off-axis eddies, respectively. The average power of the LOS component as well as that of the total scatter components are $\Omega = E[|U_L|^2]$
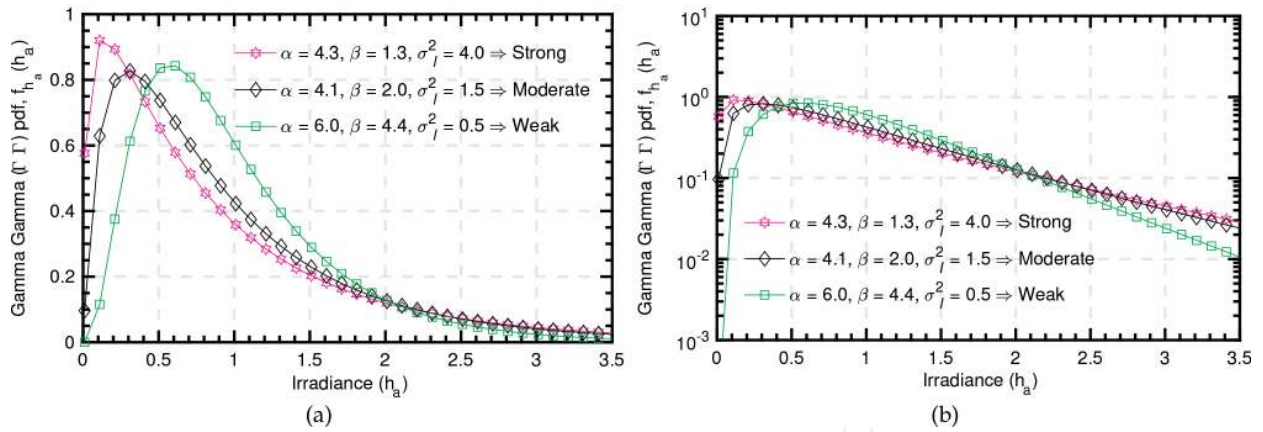
Figure 13. Gamma-gamma pdf for weak-strong turbulence regimes using (a) linear scale and (b) logarithmic scale.

Distribution model										
						Generation				
	ρ	$Var[|U_L|]$	$Var[G]$	X	Ω'	$Var[X]$	γ	Ω	α	β
Rice-Nakagami	0	0								
Gamma	0						0			
Homodyned K (HK)	0		0	γ						
Gamma-gamma	1				1		0			
Shadowed-Rician						0				
Log-normal	0	0					$\rightarrow 0$			
K	0							0		
Exponential	0	0						0	$\rightarrow \infty$	
Gamma-Rician										$\rightarrow \infty$

Adapted from Ref. [41].

Table 4. Approximations required for generating different distribution models from M-distribution model.

and $2b_0 = E[|U_S^C|^2 + |U_S^G|^2]$, respectively. In addition, the average power of the coupled-to-LOS scattering component and that of the scattering component received by off-axis eddies are $E[|U_S^C|^2] = 2\rho b_0$ and $E[|U_S^G|^2] = (1 - \rho)2b_0]$, respectively. The parameter $0 \leq \rho \leq 1$ represents the amount of scattering power coupled to the LOS component [41, 42]. The pdf of the optical channel gain h_a for the M-distribution can be written as [41, 42]

$$f_{h_a}(h_a) = A \sum_{k=1}^{\beta} a_k h_a^{\frac{\alpha+k}{2}-1} K_{\alpha-k}\left(2\sqrt{\frac{\alpha\beta h_a}{\mu\beta + \Omega'}}\right) \tag{29}$$

where $\mu = E[|U_S^C|]^2 = (1 - \rho)2b_0$, $\Omega' = \Omega + 2\rho b_0 + 2\sqrt{2\rho b_0 \Omega}cos(\varphi_A - \varphi_B)$, φ_A and φ_B represent the deterministic phases of the LOS and the coupled-to-LOS component, respectively; α denotes a positive parameter that depends on the effective number of large-scale cells of the

scattering process, β is a natural number which represents the amount of fading parameter, $K_v(\cdot)$ represents the modified Bessel function of the second kind with order v, A and a_k can be expressed, respectively, as [41, 42]

$$A \triangleq \frac{2\alpha^{\frac{\alpha}{2}}}{\mu^{1+\frac{\alpha}{2}}\Gamma(\alpha)} \left(\frac{\mu\beta}{\mu\beta + \Omega'}\right)^{\beta+\frac{\alpha}{2}} \tag{30}$$

$$a_k \triangleq \binom{\beta -1}{k -1} \frac{(\mu\beta + \Omega')^{1-\frac{k}{2}}}{(k-1)!} \left(\frac{\Omega'}{\mu}\right)^{k-1} \left(\frac{\alpha}{\beta}\right)^{\frac{k}{2}} \tag{31}$$

3.4. Combined attenuation statistics

The pdf of $h = h_\ell h_a h_p$ that constitutes the aforementioned factors of the propagation channel can be defined as [37, 38]

$$f_h(h; w_z) = \int f_{h|h_a}(h|h_a) f_{h_a}(h_a) dh_a \tag{32}$$

where $f_{h|h_a}(h|h_a)$ is the conditional probability given a turbulence state h_a and its distribution can be written as [37, 38]

$$f_{h|h_a}(h|h_a) = \frac{1}{h_a h_\ell} f_{h_p}\left(\frac{h}{h_a h_\ell}\right) = \frac{\gamma^2}{A_0^{\gamma^2} h_a h_\ell} \left(\frac{h}{h_a h_\ell}\right)^{\gamma^2 -1}, \qquad 0 \le h \le A_0 h_a h_\ell. \tag{33}$$

Therefore, $f_h(h; w_z)$ can be written as [37]

$$f_h(h; w_z) = \frac{\gamma^2}{(A_0 h_\ell)^{\gamma^2}} h^{\gamma^2 -1} \int\limits_{h/A_0 h_\ell}^{\infty} h_a^{-\gamma^2} f_{h_a}(h_a) dh_a. \tag{34}$$

4. Performance analysis

4.1. BER

The channel state distribution $f_h(h; w_z)$ can be calculated by employing an appropriate model for atmospheric turbulence regimes in Eq. (25) as follows:

1. **For a weak turbulence** $(\sigma_R^2 < 0.3)$

   In this regime, $f_{h_a}(h_a)$ follows LN distribution, so, $f_h(h; w_z)$ can be expressed as [37]

$$f_h(h; w_z) = \frac{\gamma^2}{2(A_0 h_\ell)^{\gamma^2}} h^{\gamma^2 -1} \times \text{erfc}\left(\frac{\ln\left(\frac{h}{A_0 h_\ell}\right) + \mu}{\sqrt{8}\sigma_x}\right) e^{\left(2\sigma_x^2 \gamma^2 (1+\gamma^2)\right)}. \tag{35}$$

2. **For a strong turbulence**

   This regime is characterized by the $\Gamma\Gamma$ distribution, so, $f_h(h; w_z)$ can be written as [37, 38]

$$f_h(h; w_z) = \frac{2\gamma^2(\alpha\beta)^{(\alpha+\beta)/2}}{(A_0 h_\ell)^{\gamma^2}\Gamma(\alpha)\Gamma(\beta)}h^{\gamma^2-1} \times \int_{h/A_0 h_\ell}^{\infty} h_a^{(\alpha+\beta)/2-1-\gamma^2}K_{\alpha-\beta}(2\sqrt{\alpha\beta\,h_a})dh_a. \tag{36}$$

where $K_\nu(\cdot)$ can be expressed in terms of the Meijer's G-function $G_{p,q}^{m,n}[\cdot]$ as [35]

$$K_\nu(x) = \frac{1}{2}G_{0,2}^{2,0}\left[\frac{x^2}{4}\,\middle|\,\begin{matrix}-\\(\nu/2), -(\nu/2)\end{matrix}\right]. \tag{37}$$

So, from Eq. (28), $K_{\alpha-\beta}(2\sqrt{\alpha\beta h_a})$ can be expressed as [35]

$$K_{\alpha-\beta}(2\sqrt{\alpha\beta h_a}) = \left(\frac{1}{2}\right)G_{0,2}^{2,0}\left[\alpha\beta h_a\,\middle|\,\begin{matrix}-\\ \frac{\alpha-\beta}{2}, \frac{\beta-\alpha}{2}\end{matrix}\right], \tag{38}$$

Therefore, $f_h(h)$ can be written as [38]

$$f_h(h) = \frac{\alpha\beta\gamma^2}{A_0 h_l \Gamma(\alpha)\Gamma(\beta)}\left(\frac{\alpha\beta h}{A_0 h_l}\right)^{(\alpha+\beta/2)-1} \times G_{1,3}^{3,0}\left[\frac{\alpha\beta}{A_0 h_l}h\,\middle|\,\begin{matrix}1 - \frac{\alpha+\beta}{2} + \gamma^2\\ -\frac{\alpha+\beta}{2} + \gamma^2, \frac{\alpha-\beta}{2}, \frac{\beta-\alpha}{2}\end{matrix}\right]. \tag{39}$$

The average BER, $P(e)$, in terms of $P_h(h)$ can be expressed as [38]

$$P(e) = \int_0^\infty P(e|h)f_h(h)dh. \tag{40}$$

Figure 14 shows the average BER in terms of the average SNR for BPSK over different values of turbulence strength. In this analysis, only the atmospheric turbulence effect is assumed
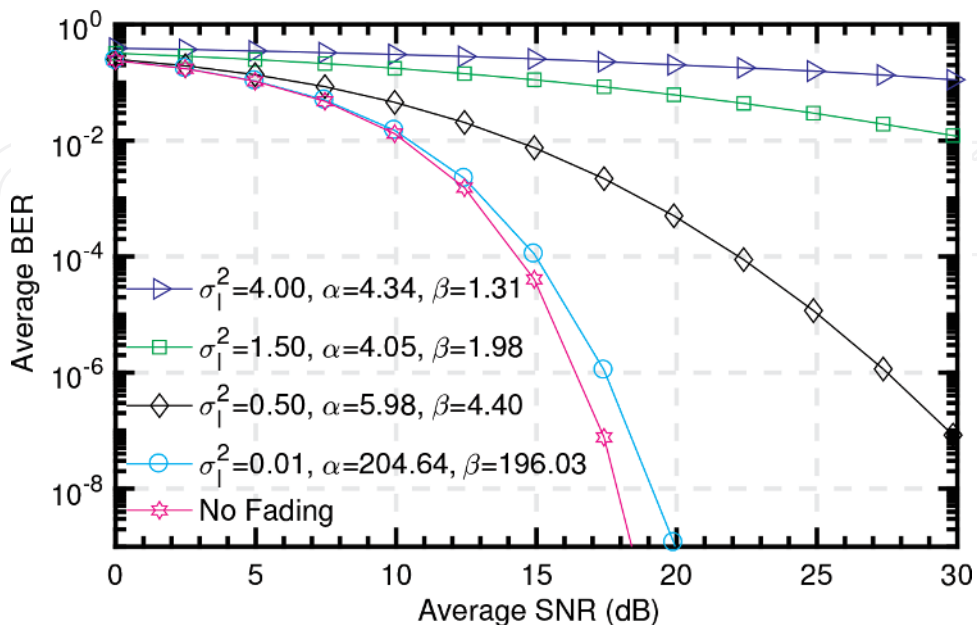

Figure 14. Average BER versus SNR for BPSK under different turbulence conditions.

when Eq. (40) is considered. The atmospheric turbulence parameters $\alpha \in$ (4.34, 4.05, 5.98, 204.64), $\beta \in$ (1.31, 1.98, 4.40, 196.03), and $\sigma_l^2 \in$ (4.00, 1.50, 0.50, 0.01), which represent weak to strong turbulence conditions, are employed in order to estimate the system BER performance. It is observed that the SNR required to achieve a specific BER increases with an increase in the atmospheric turbulence strength. For instance to achieve a BER of 10^{-6} in a channel with $\sigma_l^2 = 0.01$, the required SNR is about 18 dB; however, for fading strength of $\sigma_l^2 = 0.50$, the required SNR increases to 28 dB. Furthermore, at this BER, for $\sigma_l^2 = 0.01$ and $\sigma_l^2 = 0.50$ additional 2 and 12 dB, respectively, are required compared to the ideal channel in which there is no turbulence. This shows that the BER increases as turbulence strength becomes stronger.

4.2. Ergodic channel capacity

The channel capacity is one of the main performance metrics in the design of FSO systems that needs significant attention. The capacity of a multiple-input-multiple-output (MIMO) FSO system with M lasers and N photodetectors in bits/s/Hz can be expressed as [34]

$$C = \log_2 \left[det \left(I_M + \frac{\gamma_{inst}}{M} R \right) \right], \tag{41}$$

where $R = \begin{cases} HH^\dagger & \text{if } N < M \\ H^\dagger H & \text{if } N \leq M \end{cases}$, H denotes an $N \times M$ channel state matrix, $(\cdot)^\dagger$ corresponds to the Hermitian transpose, I_M is an $M \times M$ identity matrix, and $\gamma_{inst} = \eta_e^2 h^2 / N_0$ denotes the instantaneous electrical SNR whose average $\xi_a = \eta_e^2 \mathbb{E} \langle h \rangle^2 / N_0$.

It is worth noting that there are a number of viable approaches for the estimation of ergodic capacity of the MIMO FSO link. One of such is the numerical integration approach.

4.2.1. Numerical integration approach

The ergodic capacity, C_{erg}, of MIMO FSO link can be defined by the expected value of the instantaneous mutual information C, between the transmit and receive apertures. Hence, the C_{erg} of FSO system is a random variable and a function of SNR. The C_{erg} can be expressed as [34, 35, 43]

$$C_{erg} \triangleq \mathbb{E} \langle C \rangle = \int_0^\infty \log_2 (1 + \gamma_{inst}) f_{\gamma_{inst}} (\gamma_{inst}) d\gamma_{inst}, \tag{42}$$

where $\mathbb{E}(\cdot)$ denotes the expectation operator and $f_{\gamma_{inst}} (\gamma_{inst})$ is the pdf of γ_{inst}.

It should be noted that most of the models for ergodic capacity evaluation are based on numerical integration. However, integration-based approach requires comparatively more computational time. This is even more challenging in the strong turbulence regimes analysis. This consequence can be attributed to the Bessel function that is usually expressed in terms of the Meijer's G-function for easier evaluation [34]. In Refs. [34] and [35], computational-efficient approaches are presented in order to reduce the associated high computational time

of the integration-based approach. This enables faster performance evaluation over a wide range of SNR.

4.2.2. Power series approach

Considering the power series representation, the ergodic channel capacity can be expressed as [35]

$$\langle C \rangle = f(\mathcal{X}) = \psi \mathcal{A}(a_0 + a_1 \mathcal{X} + a_2 \mathcal{X}^2 + a_3 \mathcal{X}^3), \tag{43}$$

where $\psi = \pi/4$ and $\mathcal{A} = min\{M, N\}$ represent the minimum number of transmit or receive apertures, $\mathcal{X} = k_1 \gamma$, k_1 is a coefficient whose value is one and the unit is in b/s/Hz, and a_n represents the coefficient of the nth term given by [35]

$$a_0 = 0.13\pi k_1 \mathfrak{R}, \tag{44}$$

$$a_1 = 0.66 \mathfrak{R}, \tag{45}$$

$$a_2 = 1.45 \times 10^{-3} \mathfrak{R}, \tag{46}$$

$$a_3 = -1.73 \times 10^{-5} \mathfrak{R}, \tag{47}$$

where $\mathfrak{R} = \pi \exp(\sigma_R^2 - \sigma_N^2)$.

4.2.3. Spatial interpolation lookup approach

The spatial approach is based on B-spline and Barycentric Lagrange interpolation lookup table (B^2LUT). With the B-spline interpolated LUT, the capacity of MIMO FSO system can be expressed as [34]

$$C\left(\text{SNR}|_{(M,N,\sigma_N^2)}\right) = \sum_{t=1}^{m_1} \sum_{r=1}^{m_2} \sum_{p=1}^{m_3} \omega(\text{SNR}|_{\sigma_N^2} \mathfrak{I}_p, \cdots, \mathfrak{I}_{p+h})$$

$$\times \ \psi(\text{SNR}|_N \mathfrak{D}_r, \cdots, \mathfrak{D}_{r+\ell}) \phi(\text{SNR}|_M \mathfrak{S}_t, \cdots, \mathfrak{S}_{t+s}) \mathfrak{M}_{t,r,p}, \tag{48}$$

where $\mathfrak{I} = (\mathfrak{I}_p, \cdots, \mathfrak{I}_{p+h})$, $\mathfrak{D} = (\mathfrak{D}_r, \cdots, \mathfrak{D}_{r+\ell})$, and $\mathfrak{S} = (\mathfrak{S}_t, \cdots, \mathfrak{S}_{t+s})$ are the knot sequences, $(\mathfrak{M}_{t,r,p} : t = 1, \cdots, m_1; r = 1, \cdots, m_2; p = 1, \cdots, m_3)$ are coefficients array, and $\omega(\cdot), \psi(\cdot), \phi(\cdot)$ are the univariate piecewise B-spline for M, N, and σ_N^2, respectively.

Another main figure of merit for characterizing the communication link performance is the achievable average (ergodic) channel capacity. **Figure 15** shows the average channel capacity of FSO link as a function of average electrical SNR for different values of turbulence strength. The atmospheric turbulence parameters $\sigma_N^2 \in$ (0.0120, 0.1486, 0.2078) result in $C_N^2 \in$ ($6.03 \times 10^{-16} m^{-2/3}, 7.62 \times 10^{-15} m^{-2/3}, 1.09 \times 10^{-14} m^{-2/3}$), which correspond to the weak, moderate, and strong turbulence conditions, respectively. Moreover, the capacity of the nonturbulent channel condition (no fading) is presented for benchmarking. Obviously, the ergodic capacity of FSO link significantly depends on the atmospheric turbulence strength.
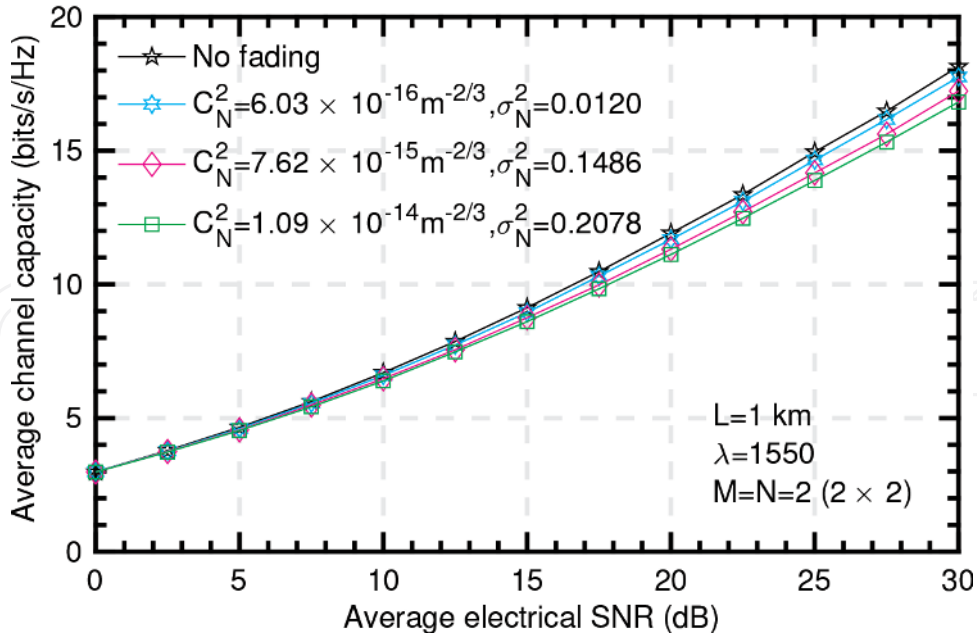
Figure 15. Average channel capacity of FSO link versus average electrical SNR.

Comparatively, the ergodic channel capacity for weak turbulence condition is considerably more than in the cases of moderate and strong turbulence conditions. Moreover, the channel condition with no fading offers the highest capacity. This shows that the atmospheric turbulence-induced fading results in severe impairment on the FSO link performance. This can eventually result in recurrent link failures. Consequently, optical wireless technologies are not as reliable as the conventional optical fiber technologies. In order to address the challenges, innovative technologies can be employed to enhance the system performance.

5. Technologies for performance enhancement

FSO is a promising optical technology that can be employed for different application. However, the tradeoff between the required high data rates and the limitations of atmospheric channel is the major challenge for reliable implementation of FSO technologies in the access networks [35]. Therefore, the problems inhibit the FSO system from being an effective and reliable standalone fronthaul technology. In this section, schemes like hybrid RF/FSO and relay-assisted transmission technologies that can be implemented to enhance the performance of FSO technology in the access networks are presented.

5.1. Hybrid RF/FSO technology

It should be noted that RF wireless technologies that operate above approximately 10-GHz frequencies are adversely affected by rain, whereas fog has insignificant effect on them. On the other hand, FSO systems are highly susceptible to fog, whereas the effect of rain on them is negligible. Therefore, it is of high importance to improve the link reliability to alleviate the adverse effects of the meteorological and weather conditions. An attractive way of addressing

the challenge is a simultaneous employment of an RF link and the FSO link for transmission. It is remarkable that fog and rain rarely occur concurrently in nature. Consequently, the two links can function in a complementary way. This concept influences the hybrid RF/FSO scheme. The RF/FSO is a hybrid scheme that combines the benefits of the inherent high transmission capacity of optical technologies and the ease of deployment of wireless links. Moreover, the idea of hybrid RF/FSO system is to concurrently attend to the related drawbacks and take advantages of both technologies. This will help in the reliable transmission of heterogeneous wireless services [8, 24].

In a hybrid RF/FSO technology, there are two parallel links between the transmitter and the receiver. Moreover, subject to deployment scenario and application, both parallel links of the hybrid technology have the capability to transmit data. Nevertheless, based on the weather conditions as well as the EMI levels, either of the links can be used for data transmission [44]. For instance, under adverse atmospheric condition (i.e., fog), the hybrid RF/FSO scheme ensures that the RF link serves as a back-up in case of FSO link outage. However, the resultant data rate of the RF link is less than that of the actual FSO link [8, 24]

5.2. Relay-assisted FSO transmission

A realistic approach for turbulence-induced fading mitigation is spatial diversity technique. In this technique, multiple transmit/receive apertures are employed in order to create and exploit additional degrees of freedom in the spatial domain. The spatial diversity is an appealing technique for fading mitigation because of its typical redundancy. However, the utilization of multiple apertures presents different challenges such as an increase in the system complexity as well as cost. In addition, the distance between the apertures has to be large enough in order to inhibit detrimental effects of spatial correlation. A simplified way of implementing spatial diversity is the dual-hop relaying which has been considerably employed in the RF communication systems. The dual-hop relaying implementation helps substantially in extending the network coverage area as well as improving the quality of the receive signal [45].

Furthermore, the concept of relay-assisted transmission is based on creating a virtual multiple-aperture system in order to realize advantages of MIMO techniques. This is achieved by exploiting both RF and FSO characteristics in order to have an efficient system in a real-life situation. Additionally, a relay-assisted transmission is also known as a mixed RF/FSO dual-hop communication scheme. The dual-hop entails the links from the source to the relay which are RF links and the links between the relay and the destination which are FSO links. In essence, RF transmission is utilized at one hop and FSO transmission is employed at the other. It is remarkable that, in principle, the mixed RF/FSO dual-hop relay scheme is comparatively different from the hybrid RF/FSO technology. In the latter, parallel RF and FSO links are normally used for the same path [45]. Furthermore, in the mixed RF/FSO dual-hop scheme, the main purpose of the FSO link is to enable the RF users to communicate with the backbone network. This helps bridging the connectivity gap between the backbone and the last-mile access networks [42, 46].

The mixed RF/FSO dual-hop model efficiently addresses the last-mile transmission bottleneck of the system. This is achieved by enabling multiplexing of multiple users with RF capabilities

as well as their aggregation in a particular high-speed FSO link so as to exploit the inherent optical capacity [42, 45]. Moreover, this implementation stalls any form of interference due to the fact that RF and FSO operate on completely different frequency bands. Therefore, the mixed RF/FSO dual-hop model offers better performance compared to the traditional RF/RF transmission system [45, 46]. In a mixed RF/FSO system, the source comprises multiple RF users, each equipped with an antenna. Furthermore, at the destination, there is an FSO detector that is equipped with an aperture. In addition, the source and the destination are connected by a relay that is usually mounted on a high platform. The relay node performs RF to FSO conversion. Also, the relay has a receive antenna and a transmit aperture that are assigned for the RF signal reception and optical signal transmission, respectively.

6. Channel measurement and characterization

In this section, the performance of an FSO link subjected to a real atmospheric turbulence condition is investigated experimentally. The σ_N^2 is measured from the channel samples obtained so as to determine the degree of atmospheric turbulence and the subsequent effects on the FSO link quality. Furthermore, the C_n^2 can be calculated as explained in Section 3.

6.1. Experimental setup

The experimental setup shown in **Figure 16** is employed in the channel measurement. The setup consists of a point-to-point FSO link that is based on IM/DD technique. The pattern generator uses a pseudorandom binary sequence (PRBS) of length $2^{23} - 1$ bits to generate a 10-Gb/s non-return-to-zero (NRZ) signal. Also, the produced electrical signal is then injected into a JDSU Integrated Laser Mach Zehnder (ILMZ) drives at 1548.51-nm wavelength. A standard single-mode fiber (SSMF) is used to convey the optical output signal launched from the laser to a 3-mm diameter collimator. The optical power at the input of collimator is set to 0 dBm. The collimated laser beam is subsequently transmitted over the FSO channel with a round trip length of 54 m. **Figure 16** inset depicts an outdoor FSO setup employed in the measurement. The overall transmission distance is achieved when the optical signal from collimator 1 passes
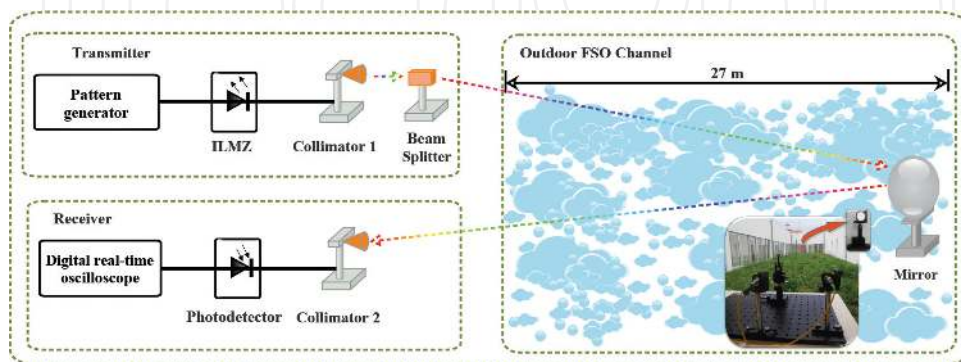
Figure 16. Experimental setup. The inset presents the picture of outdoor FSO setup, ILMZ: Integrated Laser Mach Zehnder.

through the FSO channel to the mirror with a beam diameter of about 2 cm located at the other side of the link that is 27 m long, and then reflected back to the collimator 2 at the receiver with approximately its initial diameter. The collimator is made of a concave mirror, in order to lessen beam scattering and considerably maximize the power transfer. The converged received optical signal at the receiver then focuses on the laser collimator which is coupled to the photodetector by the SSMF. The resulting optical signal is then converted into electrical signal using a 10-Gb/s PIN photodiode. The PIN is followed by a real-time sampling oscilloscope (Tektronix: DPO72004B) with a sample rate of 50 GS/s.

6.2. Experimental results

The results of FSO channel samples collected from November 9 to 20, 2015, for characterization are presented. The data obtained on November 12, 2015, at 01:45 pm and 09:30 pm are analyzed in this work. The recorded weather conditions are as follows:

1. Scenario 1: 01:45 pm

    Temperature, 22°C; wind, 6 mph; humidity, 69%; pressure, 1031 mb; visibility, 10 km; precipitation, 0 mm; and rain rate, 0%.

2. Scenario 2: 09:30 pm

    Temperature, 17°C; wind, 4 mph; humidity, 80%; pressure, 1030 mb; visibility, 9 km; precipitation, 0 mm; and rain rate, 0%.

The FSO channel measurement is realized by injecting an unmodulated optical wave that emanates from the laser into the FSO channel. The FSO channel brings about a path loss with
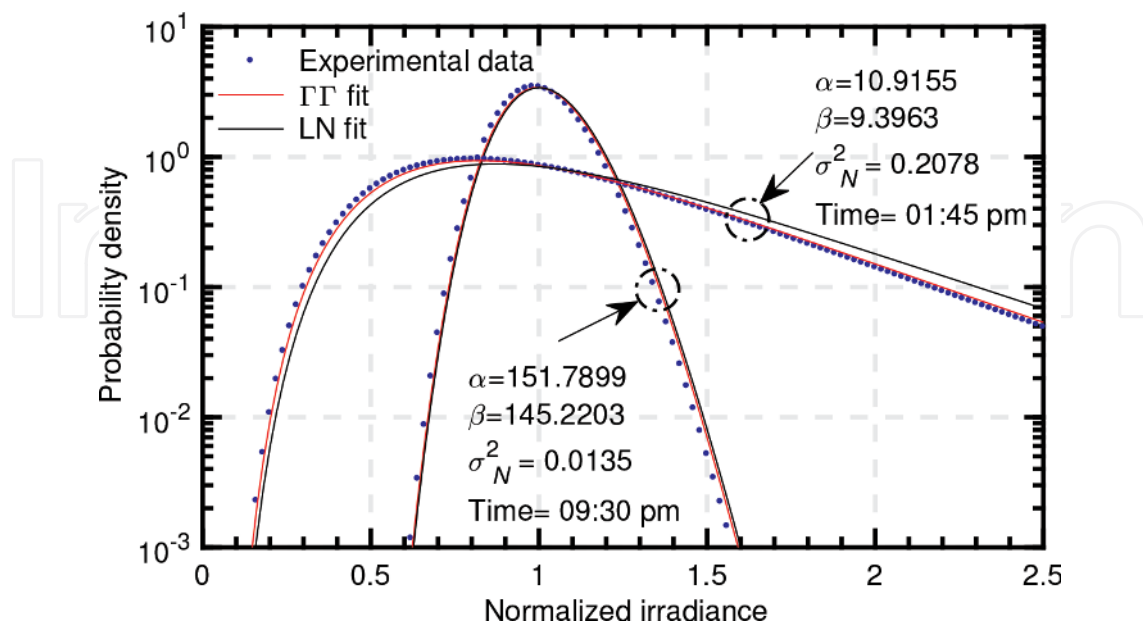
Figure 17. Histogram of normalized irradiance with log-normal and gamma-gamma fits under different scintillation index values.

a mean value of 9 dB, for the setup and the atmospheric conditions. Using statistical means, the resultant signal detected and received by the real-time oscilloscope is analyzed offline using MATLAB®.

The characterization of the refractive-index structure parameter C_n^2 is achieved by fitting the nearest LN and the ΓΓ pdf curves to the pdf of the received data. The fittings are presented in **Figure 17**. The scintillation index σ_N^2 is measured for the two scenarios considered. The values obtained are 0.0135 and 0.2078 for 09:30 pm and 01:45 pm, respectively. For the first scenario with $\sigma_N^2 = 0.0135$, the LN and the ΓΓ fit very well with the measured channel samples σ_N^2. However, when $\sigma_N^2 = 0.2078$, the LN fitting is loose and unable to give an accurate result for the fading model, whereas the ΓΓ fitting still maintains a relatively better result for the fading model. This result shows that the LN model is unsuitable for the strong atmospheric fading characterization.

Furthermore, the estimated values of the refractive-index structure parameters, C_n^2, are $6.7807 \times 10^{-16} m^{-2/3}$ ($\sigma_N^2 = 0.0135$) and $1.0864 \times 10^{-14} m^{-2/3}$ ($\sigma_N^2 = 0.2078$). Therefore, the first ($\sigma_N^2 = 0.2078$) and the second ($\sigma_N^2 = 0.0135$) scenarios correspond to the strong and weak turbulence regimes, respectively.

7. Real-time coherent PON OWC based on dual polarization for the mobile backhaul/fronthaul

In this section, proof-of-concept gigabit-capable long-reach coherent PON and OWC systems with the ability to support different applications over a shared optical fiber infrastructure are experimentally implemented. This is in an effort to demonstrate the FSO application in certain areas in the mobile cellular systems in which physical connections by means of optical fiber cables are impractical or in rural area that lacks fiber infrastructure. Moreover, this is achieved by a reconfigurable real-time DSP reception of a dual-polarization-quadrature phase shift keying (DP-QPSK) signal over the SSMF and FSO systems. It is worth noting that the system is validated by a commercial field-programmable gate array (FPGA) in order to have an open system whose components and protocols conform to standards independent of a particular equipment vendor. In this analysis, we study signal transmission and reception over 100 km of SSMF as well as over a hybrid 100 km of SSMF plus a 54-m outdoor FSO link. We are able to establish the lowest sampling rate that is necessary for digital coherent PON by employing four 1.25 Gsa/s ADCs with an electrical front-end receiver that offers just 1-GHz analog bandwidth. This is realized by implementing a phase and polarization diversity coherent receiver in conjunction with the DP-QPSK modulation formats. This technique is of high importance in order to relax the required electrical digital units at the optical network unit (ONU) toward the RF rates. This scheme also helps in realizing the anticipated data rate for the next-generation coherent optical access networks for the 5G Mobile wireless networks.

7.1. Experimental setup

The experimental setup depicted in **Figure 18a** is used to validate the performance of a PON system with hybrid fiber and FSO link using DP signals. It is worth mentioning that only the
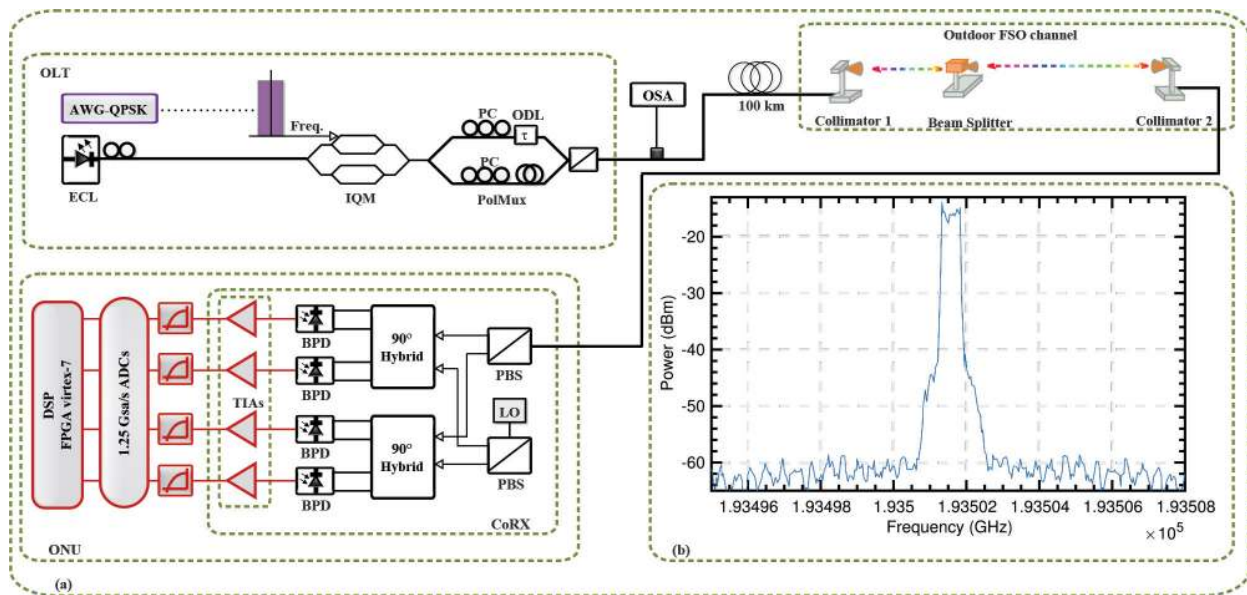
Figure 18. (a) Experimental setup for 20×625 Mbaud DP-QPSK signal; (b) Overall spectrum (PBS: polarization beam splitter; BPD: balanced photodetector; CoRX: coherent receiver).

receiver DSP of the setup is estimated in real time. At the OLT, the light from an external cavity laser (ECL) (<100 kHz linewidth) is injected into an IQ modulator (IQM). The wavelength λ is centered at ~1549 nm. The IQM is driven by a 65-Gsa/s arbitrary waveform generator (AWG) that generates 625 Mbaud signals from a $2^{12} - 1$ pseudo random bit sequence (PRBS). The subsequent signal is then digitally filtered using a raised-cosine (RC) filter with a 0.1-roll-off factor and 32-taps FIR resolution in addition to a simple 3-taps FIR pre-emphasis subsystem. The employed modulation format is the differential DP-QPSK, providing 2.5 Gb/s per end user. The obtained spectrum is shown in **Figure 18b**.

In an effort to emulate the DP system, this signal is divided into two using an optical splitter. Then, we applied a delay of 12 symbols to one of them for an effective decorrelation purposes. Afterward, both polarized signals are multiplexed orthogonally once again using a polarization beam combiner (PBC). This implementation results in dual polarization of the signal. The optical power is managed using variable optical attenuators (VOAs). This subsequent signal is then propagated over 100 km of an SSMF and 54-m FSO. At the receiver side, the signal is coherently detected using a 4×90° optical hybrid by means of a free-running ECL LO with about 100-kHz linewidth tuned to the center channel, λ. The optical signal is converted to the electrical domain using four balanced detectors (BDs) and then amplified by transimpedance amplifiers (TIAs). This results in the in-phase and quadrature components of each polarization. It is worth noting that only an output of the TIA is used. The signal is then filtered using a 1-GHz low-pass filter and sampled by four 8-bit 1.25 Gsa/s ADCs. The digitalized signal is conveyed to a Virtex-7 FPGA, where the entire post-detection 8-bit DSP in real time is implemented. The applied DSP is based on [47]. The bit-error rate (BER) is calculated in real time by bit error counting, averaged between the two polarizations.

In addition, we consider the possibility of an outdoor FSO communication link as part of the system. The employed FSO link setup in this study is similar to that in **Figure 16** that we have
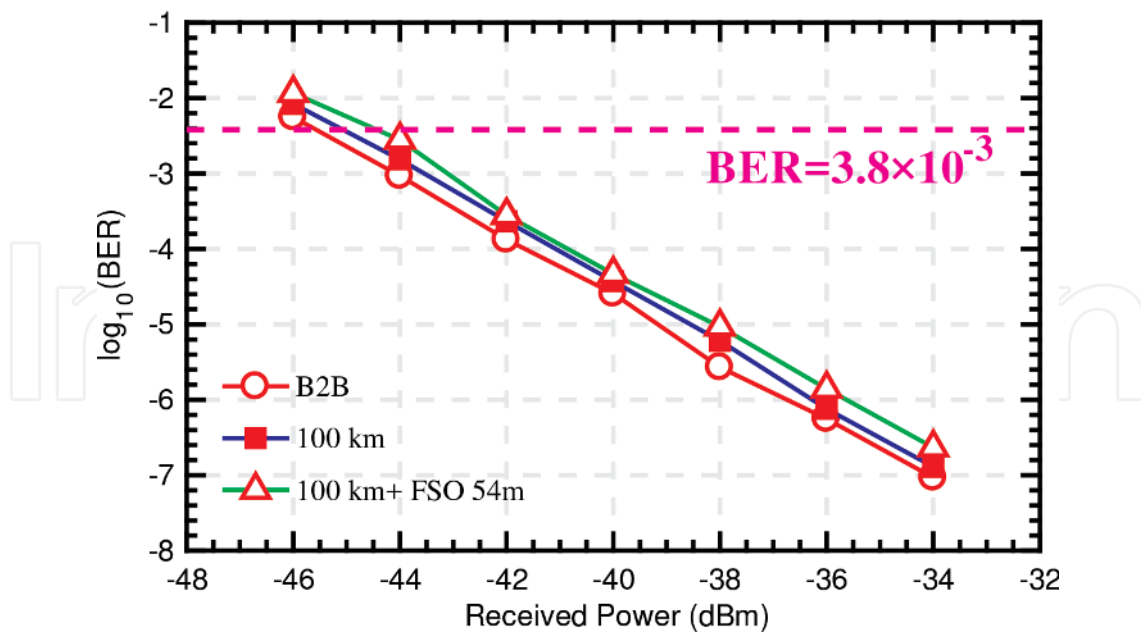
Figure 19. Receiver sensitivity in terms of BER measured for DP-QPSK signals.

discussed in Section 6. The outdoor FSO link experiences a total loss of ~8–9 dBm. At the collimator, the received signal is guided to an integrated phase- and polarization-diverse coherent receiver.

7.2. Experimental results

Figure 19 illustrates receiver sensitivity in terms of BER measured for the DP-QPSK signal. The figure presents results for the back-to-back (B2B) and 100 km of fiber scenarios as well as 100-km plus 54-m FSO. The considered BER limit of 3.8×10^{-3} corresponds to the 7% hard-decision forward error correction (HD-FEC). As shown in **Figure 19**, there is no significant penalty between 100 and 100-km plus FSO in real-time results.

8. Conclusions

In this chapter, we have presented various opportunities of using optical wireless communication technology for addressing the last-mile transmission bottleneck of the fixed/mobile network. We have also discussed various challenges of the OWC and presented different solutions in order to make OWC an efficient technology. In the proof-of-concept experiment, we study the transmission capabilities of a PON based on DP signal in terms of receiver sensitivity. This is implemented with the real-time ONU receiver that is emulated by a commercial FPGA. This helps in facilitating an open system and hence enables interoperability, portability, and open software standards. The transmissions over 100 km of SSMF as well as over a hybrid 100 km of SSMF plus a 54-m outdoor FSO link are successfully realized considering 625 Mbaud DP-QPSK channel.

Acknowledgements

Author details

Isiaka Alimi*, Ali Shahpari, Artur Sousa, Ricardo Ferreira, Paulo Monteiro and António Teixeira

*Address all correspondence to: iaalimi@ua.pt

Instituto de Telecomunicações, Department of Electronics, Telecommunications and Informatics, Universidade de Aveiro, Aveiro, Portugal

References

[1] Yu C, Yu L, Wu Y, He Y, Lu Q. Uplink scheduling and link adaptation for narrowband internet of things systems. IEEE Access, 2017;**5**:1724–1734

[2] Ejaz W, Anpalagan A, Imran MA, Jo M, Naeem M, Qaisar SB, Wang W. Internet of things (IoT) in 5G wireless communications. IEEE Access. 2016;**4**:10310–10314

[3] Alimi I, Shahpari A, Ribeiro V, Kumar N, Monteiro P, Teixeira A. Optical wireless communication for future broadband access networks. In: 2016 21st European Conference on Networks and Optical Communications (NOC); IEEE; Lisbon, Portugal. Jun 2016. pp. 124–128

[4] Parca G, Tavares A, Shahpari A, Teixeira A, Carrozzo V, Beleffi GT. FSO for broadband multi service delivery in future networks. In: 2013 2nd International Workshop on Optical Wireless Communications (IWOW); IEEE; Newcastle upon Tyne, UK. Oct 2013. pp. 67–70

[5] Ghassemlooy Z, Popoola W, Rajbhandari S. Optical wireless Communications: System and Channel Modelling with MATLAB®. Taylor & Francis; London, New York: 2012

[6] Ghassemlooy Z, Amon S, Uysal M, Xu Z, Cheng J. Emerging optical wireless communications-advances and challenges. IEEE Journal on Selected Areas in Communications. Sep 2015;**33**(9):1738–1749

[7] Alkholidi AG, Altowij KS. Free Space Optical Communications—Theory and Practices, Contemporary Issues in Wireless Communications. InTech; 2014. pp. 159–212

[8] Khalighi MA, Uysal M. Survey on free space optical communication: A communication theory perspective. IEEE Communications Surveys Tutorials. 2014;**16**(4):2231–2258

[9] Bloom S, Korevaar E, Schuster J, Willebrand H. Understanding the performance of free-space optics [Invited]. Journal of Optical Network. Jun 2003;**2**(6):178–200

[10] Kaushal H, Kaddoum G. Optical communication in space: Challenges and mitigation techniques. IEEE Communications Surveys Tutorials. 2017;**19**(1)57–96

[11] Zeng Z, Fu S, Zhang H, Dong Y, Cheng J. A survey of underwater optical wireless communications. IEEE Communications Surveys Tutorials. 2017;**19**(1):204–238

[12] Pompili D, Akyildiz IF. Overview of networking protocols for underwater wireless communications. IEEE Communications Magazine. Jan 2009;**47**(1):97–102

[13] Sevincer A, Bhattarai A, Bilgi M, Yuksel M, Pala N. FIGHTNETs: Smart FIGHTing and mobile optical wireless NETworks—A survey. IEEE Communications Surveys Tutorials. Fourth 2013;**15**(4):1620–1641

[14] Rajagopal S, Roberts RD, Pirn SK. IEEE 802.15.7 visible light communication: Modulation schemes and dimming support. IEEE Communications Magazine. Mar 2012;**50**(3):72–82

[15] Ying K, Yu Z, Baxley RJ, Qian H, Chang GK, Zhou GT. Nonlinear distortion mitigation in visible light communications. IEEE Wireless Communications. Apr 2015;**22**(2):36–45

[16] Yang F, Gao J. Dimming control scheme with high power and spectrum efficiency for visible light communications. IEEE Photonics Journal. Feb 2017;**9**(1):1–12

[17] Pinterest. Color wavelength frequency. Feb 2017. [Online]. Available from: https://www.pinterest.com/pin/408983209884752740/.

[18] Wang M, Wu J, Yu W, Wang H, Fi J, Shi J, Fuo C. Efficient coding modulation and seamless rate adaptation for visible light communications. IEEE Wireless Communications. Apr 2015;**22**(2):86–93

[19] ANDY. Visible Light Communication—VLC & PUREVLC™. February 2017 [Online]. Available from: http://andy96877.blogspot.pt/p/visible-light-communication-vlc-is-data.html

[20] Jan SU, Fee YD, Koo I. Comparative analysis of DIPPM scheme for visible light communications. In: 2015 International Conference on Emerging Technologies (ICET); IEEE; Peshawar, Pakistan. Dec 2015. pp. 1–5

[21] Tsouri GR, Zambito SR, Venkataraman J. On the benefits of creeping wave antennas in reducing interference between neighboring wireless body area networks. IEEE Transactions on Biomedical Circuits and Systems. Feb 2017;**11**(1):153–160

[22] Zhang R, Moungla H, Yu J, Mehaoua A. Medium access for concurrent traffic in wireless body area networks: Protocol design and analysis. IEEE Transactions on Vehicular Technology. Mar 2017;**66**(3):2586–2599

[23] Cahyadi WA, Jeong TI, Kim YH, Chung YH, Adiono T. Patient monitoring using visible light uplink data transmission. In: 2015 International Symposium on Intelligent Signal Processing and Communication Systems (ISPACS); IEEE; Nusa Dua, Indonesia. Nov 2015. pp. 431–434

[24] Uysal M, Capsoni C, Ghassemlooy Z, Boucouvalas A, Udvary E. Optical wireless communications: An emerging technology. Signals and Communication Technology. Springer International Publishing; Switzerland: 2016

[25] Baister G, Gatenby PV. Pointing, acquisition and tracking for optical space communications. Electronics Communication Engineering Journal. Dec 1994;**6**(6):271–280

[26] Toyoshima M. Trends in satellite communications and the role of optical free-space communications [Invited]. Journal of Optical Networking. Jun 2005;**4**(6):300–311

[27] D'Amico M, Feva A, Micheli B. Free-space optics communication systems: First results from a pilot field-trial in the surrounding area of Milan, Italy. IEEE Microwave and Wireless Components Letters. Aug 2003;**13**(8)505–307

[28] Song D-Y, Hurh Y-S, Cho J-W, Lim J-H, Fee D-W, Fee J-S, Chung Y. 4 × 10 Gb/s terrestrial optical free space transmission over 1.2 km using an EDFA preamplifier with 100 GHz channel spacing. Optics Express. Oct 2000;**7**(8):280–284

[29] Carlson RT, Paciorek S. Environmental Qualification and Field Test Results for the SONAbeam™ 155 and 622. Technical Report, fSONA Communications Corp. 2017; http://www.fsona.com/tech/white_papers/tech_qual-test.pdf

[30] Bandera P. Defining a Common Standard for Evaluating and Comparing Free-Space Optical Products. Technical Report, fSONA Communications Corp. 2017; http://www.fsona.com/tech/white_papers/WHTPAP-Generalized_Link_Margin.pdf

[31] LightPointe. Ultra-Low Latency Point-to-Point Wireless Bridge. White Paper, [Online]. Available from: http://nebula.wsimg.com/793e82b2beac48cb90c347bd86776d12?AccessKeyId=C1431E109BF92B03DF85&disposition=0&alloworigin=1.

[32] Wang Z, Zhong WD, Fu S, Fin C. Performance comparison of different modulation formats over free-space optical (FSO) turbulence links with space diversity reception technique. IEEE Photonics Journal. Dec 2009;**1**(6):277–285

[33] Navidpour SM, Uysal M, Kavehrad M. BER performance of free-space optical transmission with spatial diversity. IEEE Transactions on Wireless Communications. Aug 2007;**6**(8):2813–2819

[34] Alimi IA, Abdalla AM, Rodriguez J, Monteiro PP, Teixeira AF. Spatial interpolated lookup tables (FUTs) models for ergodic capacity of MIMO FSO systems. IEEE Photonics Technology Letters. Apr 2017;**29**(7)583–586

[35] Alimi I, Shahpari A, Ribeiro V, Sousa A, Monteiro P, Teixeira A. Channel characterization and empirical model for ergodic capacity of free-space optical communication link. Optics Communications. 2017;**390**:123–129

[36] Naboulsi MA, Sizun H, de Fornel F. Fog attenuation prediction for optical and infrared waves. Optical Engineering. 2004;**43**(2):519–329

[37] Farid AA, Hranilovic S. Outage capacity optimization for free-space optical links with pointing errors. Journal of Lightwave Technology. Jul 2007;**25**(7):1702–1710

[38] Sandalidis HG, Tsiftsis TA, Karagiannidis GK. Optical wireless communications with heterodyne detection over turbulence channels with pointing errors. Journal of Lightwave Technology. Oct 2009;**27**(20):4440–4445

[39] Andrews FC, Phillips RF. Laser Beam Propagation through Random Media. Press Monographs. SPIE Press; Bellingham, Washington USA. 2005

[40] Kiasaleh K. Performance of APD-based, PPM free-space optical communication systems in atmospheric turbulence. IEEE Transactions on Communications. Sep 2005;**53**(9):1455–1461

[41] Jurado-Navas A, Garrido-Balsells JM, Paris JF, Puerta-Notario A. A Unifying Statistical Model for Atmospheric Optical Scintillation. InTech; Rijeka, Croatia. 2011. pp. 181–206

[42] Yang F, Hasna MO, Gao X. Performance of mixed RF/FSO with variable gain over generalized atmospheric channels. IEEE Journal on Selected Areas in Communication. Sep 2015;**33**(9):1913–1924

[43] Peppas KP, Stassinakis AN, Topalis GK, Nistazakis HE, Tombras GS. Average capacity of optical wireless communication systems over I-K atmospheric turbulence channels. IEEE/OSA Journal of Optical Communications and Networking. Dec 2012;**4**(12):1026–1032

[44] Dahrouj H, Douik A, Rayal F, Al-Naffouri TY, Alouini MS. Cost-effective hybrid RF/FSO backhaul solution for next generation wireless systems. IEEE Wireless Communications. Oct 2015;**22**(5):98–104

[45] Zhang J, Dai F, Zhang Y, Wang Z. Unified performance analysis of mixed radio frequency/free-space optical dual-hop transmission systems. Journal of Lightwave Technology. Jun 2015;**33**(11):2286–2293

[46] Ansari IS, Yilmaz F, Alouini MS. Impact of pointing errors on the performance of mixed RF/FSO dual-hop transmission systems. IEEE Wireless Communications Letters. Jun 2013;**2**(3) 551–354

[47] Ferreira RM, Shahpari A, Reis JD, Teixeira AF. Coherent UDWDM-PON with dual-polarization transceivers in real-time. IEEE Photonics Technology Letters. Jun 2017;**29**(11):909–912